

REPORT DOCUMENTATION PAGE

Form Approved
OMB No. 0704-0188

Public reporting burden for this collection of information is estimated to average 1 hour per response, including the time for reviewing instructions, searching data sources, gathering and maintaining the data needed, and completing and reviewing the collection of information. Send comments regarding this burden estimate or any other aspect of this collection of information, including suggestions for reducing this burden to Washington Headquarters Service, Directorate for Information Operations and Reports, 1215 Jefferson Davis Highway, Suite 1204, Arlington, VA 22202-4302, and to the Office of Management and Budget, Paperwork Reduction Project (0704-0188) Washington, DC 20503.

PLEASE DO NOT RETURN YOUR FORM TO THE ABOVE ADDRESS.

1. REPORT DATE (DD-MM-YYYY) 08-03-2005	2. REPORT DATE Final Report	3. DATES COVERED (From - To) Sep-2003-Nov-2004		
4. TITLE AND SUBTITLE Development of Soft Magnetic Films for Thin Film Inductor for High Frequency Applications.		5a. CONTRACT NUMBER N00014-03-1-0819		
		5b. GRANT NUMBER		
		5c. PROGRAM ELEMENT NUMBER		
		5d. PROJECT NUMBER		
		5e. TASK NUMBER		
		5f. WORK UNIT NUMBER		
7. PERFORMING ORGANIZATION NAME(S) AND ADDRESS(ES) University of Idaho Moscow, ID 83844		8. PERFORMING ORGANIZATION REPORT NUMBER		
9. SPONSORING/MONITORING AGENCY NAME(S) AND ADDRESS(ES)		10. SPONSOR/MONITOR'S ACRONYM(S)		
		11. SPONSORING/MONITORING AGENCY REPORT NUMBER		
12. DISTRIBUTION AVAILABILITY STATEMENT	DISTRIBUTION STATEMENT A Approved for Public Release Distribution Unlimited			
13. SUPPLEMENTARY NOTES				
14. ABSTRACT See Attached Final Report				
15. SUBJECT TERMS Thin Film Inductor, High Magnetic Moment, High Permeability,				
16. SECURITY CLASSIFICATION OF: a. REPORT b. ABSTRACT c. THIS PAGE		17. LIMITATION OF ABSTRACT	18. NUMBER OF PAGES 53	19a. NAME OF RESPONSIBLE PERSON Hong, Yang-Ki
				19b. TELEPHONE NUMBER (Include area code) 208-885-5915

I. Executive Abstract

The goals of the program was to develop soft magnetic films, fabricate test structures, to device a microwave inductor and integrate thin film inductor onto CMOS (complimentary metal oxide semiconductor). Six researchers from four different academic departments including materials science, physics, chemical engineering and electrical engineering have conducted their own research projects. This report contains six sub-reports for detailed information on the results.

II. Technical Program

Development of High Resistive and High Magnetization Soft Thin Film and Fabrication of Thin Film Inductors

Yang-Ki Hong

Department of Materials Science and Engineering

I. Abstract

Soft magnetic $(Fe_xCo_{1-x})_yM_z$ alloy thin films were prepared by dc magnetron sputtering for chip inductor gigahertz band applications. The effects of substrates bias, sputter parameters, and seed-layer have thoroughly been investigated. The magnetic properties of $(Fe_xCo_{1-x})_yM_z$ alloy films were characterized using vibrating sample magnetometer (VSM), B-H loop tracer, superconducting quantum interference device (SQUID). The physical properties of alloy films, which include composition, structural properties, and film morphology, were examined by X-ray diffractometer (XRD), high resolution transmission electron microscopy (HRTEM), selected area diffraction (SAD), and energy dispersive X-rays (EDX).

Substrate bias effects on soft magnetic properties of 200 nm thick Fe-10%Co alloy films have been investigated by dc magnetron sputtering on both (100) silicon and (111) MgO substrates. An average saturation magnetization of the films increased from 17.2 to 24.1 kG by applying 200 V substrate bias, while the coercivity of the film deposited on the silicon (Si) decreased to 19 Oe from 159 Oe of unbiased films. Both biased and unbiased films showed bcc structure from x-ray diffraction pattern. However, the biased film had well-defined columnar structure with 20 nm in diameter discovered by using HRTEM and SAD, but the unbiased film showed randomly oriented crystallites existing near the interface between the film and substrate. The magnetostriction (λ) of Fe-10%Co alloy film was 1.89×10^{-5} with 300 V biased. The coercivity of a substrate biased film was further decreased to 2.8 Oe with 2.5 nm of Co seed-layer. In order to improve soft magnetic properties of Fe-10%Co alloy film, 1% Al_2O_3 was added into a Fe-10%Co sputtering target. The properties of $(Fe-10\%Co)_{99}(Al_2O_3)_1$ film were 390 Oe, $28 \mu\Omega\text{-cm}$, and 9 Oe for anisotropy field (H_k), resistivity, and coercivity, respectively. Adequate properties of soft magnetic thin film were evaluated by an analytical calculation [1] to meet the requirement for gigahertz band thin-film inductor application. The calculated ferromagnetic resonance frequency (FMR) was 7.9 GHz using those values of $(Fe-10\%Co)_{99}(Al_2O_3)_1$ alloy film.

Finally, the design and detail of fabrication procedure of thin film inductor was introduced. A four turn copper tracer was fabricated on a silicon wafer using electron beam lithography.

II. Approach and Results

- Development of soft magnetic materials for gigahertz frequency range.

There have been many attempts to optimize the magnetic and physical properties of soft magnetic film with the applications of microchip inductors in rf (radio frequency)

integrated circuits [2-17]. One of the main factors to determine frequency response is the ferromagnetic resonance (FMR), which must be higher than the maximum operational frequency. The FMR frequency is proportional to the square root of the anisotropy field (H_k) multiple the saturation magnetization ($4\pi M_s$), expressed by equation (1), where f_r and γ represent FMR frequency and the gyromagnetic ratio (1.76×10^7 rad/Oe), respectively. On the other hand, permeability (μ'_{dc}) increases with the increase of $4\pi M_s$ and with the decrease of H_k , expressed by equation (2). Therefore, there is a trade off between saturation magnetization and anisotropy field for a given permeability [1].

$$f_r = \frac{\gamma}{2\pi} \sqrt{H_k 4\pi M_s} \quad (1)$$

$$\mu'_{dc} = 1 + \frac{4\pi M_s}{H_k} \quad (2)$$

Since the Fe-Co alloy system is known to have the highest saturation magnetization [2], there has been research to develop high frequency soft magnetic films using Fe-Co alloys thin films by adding dopants [3-5], post-annealing [6], underlayers [7-10], and applied bias voltage [11, 12]. For FeCoB film, the properties are permeability μ' of 200, and FMR frequency, 3.3 GHz. S. X. Wang *et al.* developed sandwiched FeCo nitride with NiFe films [4, 7, 13]. H. Jiang *et al.* also reported FeCoN films with high moment and high resistivity [14]. The FMR frequency of FeCoN film with $\mu' = 1200$ reached to 2 GHz [4]. S. Ohnuma and K. Shintaku *et al.* improved resistivity and soft magnetic properties with an addition of small amount of aluminum oxide in Fe-Co alloy films [15, 16]. N. A. Lesnik *et al.* fabricated $(Fe_{50}Co_{50})_x(Al_2O_3)_{1-x}$ using an electron beam evaporation technique at oblique incident of FeCo and alumina atom flux [17].

Substrate bias during sputter deposition has been an important parameter for the control of nucleation and growth of thin films [18]. A combination of 300 V of substrate bias and magnetic annealing has improved soft properties of $Fe_{49}Co_{49}V_2$ from about 170 to 10 Oe [10]. However, the substrate bias has led to the oxidation of grain boundaries, resulting in an increase of coercivity and decrease in saturation magnetization of $Fe_{35}Co_{65}$ [11]. In the research work, newly developed $(Fe_xCo_{1-x})_yM_z$ alloy films with substrate bias have been studied on magnetic and physical properties of films and compared with the analytical model that was estimated to be applicable up to 7.9 GHz of FMR frequency.

- Deposition of Fe-Co alloy films with substrate bias.

The Fe-Co alloy films were deposited on both a naturally oxidized silicon (100) substrate and MgO (111) single crystal substrate at room temperature using dc magnetron sputtering with a working pressure of 5 mTorr. The applied dc power density of the target was 10 watt/cm², and a bias voltage was applied on the substrate in the range of zero and 300 volts to the substrate holder. Commercially available stoichiometric Fe-Co alloy 2 inch targets (Williams Advanced Materials Inc.) were used to grow the films: the composition of targets varied from 5 to 50 atomic percent of cobalt in iron matrix. The saturation magnetization of bulk specimens were cut from the used target materials to compare with the saturation magnetization of deposited Fe-Co films. In order to improve in soft properties and increase the resistivity of Fe-Co films, 1% Al₂O₃ to Fe-10%Co target, $(Fe-10\%Co)_{99}(Al_2O_3)_1$ was deposited on (100) silicon wafer.

Substrate bias sputtering is defined to apply bias potential to the substrate during dc sputtering deposition. The common feature of bias sputter deposition is the introduction of ion bombardment at the surface of a growing film by imposition of negative potential relative to the plasma. Positive ions from the plasma are accelerated across the sheath created by the substrate bias and impart sufficient energy to the film that atomic rearrangements, including enhanced resputtering and recoil bombardment, are promoted. This normally improves the quality of the deposited film, due partly to a low energy ion bombardment of the growing film that may preferentially remove loosely bonded atoms or molecules from the surface [19]. The energy released by low energy ions to the surface may also increase the surface mobility of the incoming atoms. The normal energy of the substrate bombarding ions in bias sputtering is in the range of 50 to 150 eV. The use of substrate bias in dc depositions is historically the first attempt to control film properties through particle bombardment of the growing film [19]. Thornton proposed using the resputter fraction as a fundamental measure of the deposited energy required to control film morphology and properties [20]. The earliest applications of bias sputtering arose from a desire to minimize the gaseous impurity content of thin resistive films whose properties were greatly influenced by the bombardment of reactive gases [22]. The mechanism for the beneficial removal of contaminants from the film surface through use of substrate bias has been attributed to the preferential resputtering of the atomically lighter impurity species, such as oxygen and nitrogen, from the growing film surface [23]. Thornton also discussed the morphological changes accompanying bias deposition of copper films in a hollow cathode system at various pressures [20]. Jones *et al.* observed that resputtering associated with biased deposition of film material promoted densification of films for rf sputtered SiO_2 [18]. The elimination of reactive contaminants during bias bombardment should promote both adatom diffusion process and recoil implantation of adatoms in the void regions [19]. Mattox and co-workers obtained direct evidence for microstructural changes occurring with bias sputtering [18]. A combination of 300 V of substrate bias and magnetic annealing has improved soft magnetic properties of $\text{Fe}_{49}\text{Co}_{49}\text{V}_2$ from about 170 to 10 Oe [23]. In this report, substrate bias effects have been investigated on saturation magnetization and soft magnetic properties of $(\text{Fe}_x\text{Co}_{1-x})_y\text{M}_z$ alloy thin films for GHz range thin-film inductor application.

III. Conclusions

Figure 1 shows substrate bias effects on saturation magnetic flux density ($4\pi M_s$) of $\text{Fe}_{100-x}\text{Co}_x$ ($10 \leq x \leq 50$) films, which thickness of films are between 150 to 250 nm. The saturation magnetization of bulk specimens were cut from the used sputter target materials. The substrate bias significantly influences the saturation magnetization of Fe-Co alloy films in the all composition range. The saturation magnetization of biased films is higher than that of unbiased ones by 17.5 to 25%, while the coercivity of the one deposited on the Si decreased to 19 Oe from 159 Oe of unbiased films. In addition, two data points of VSM measurement were confirmed from SQUID measurement to remove the error from VSM measurement.

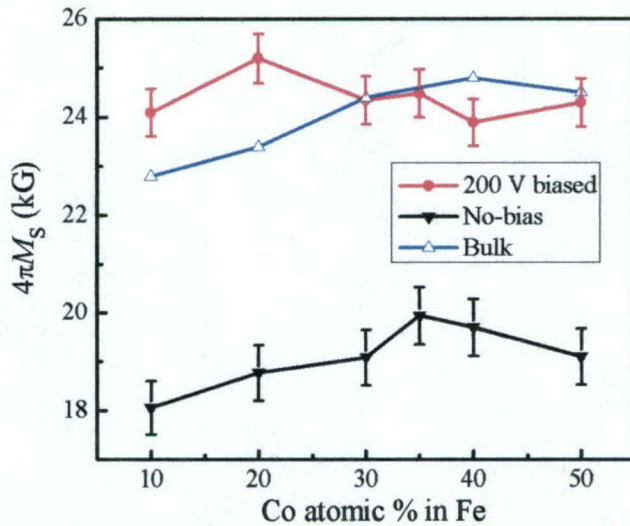


Figure 1. Substrate bias effects on saturation magnetic flux density ($4\pi M_s$) of $\text{Fe}_{100-x}\text{Co}_x$ ($10 \leq x \leq 50$) films.

In order to verify the accuracy of VSM, Fig. 2 shows that the variation of saturation magnetization of pure Nickel foil, Alfa Aesar ®, with known emu/g as a function of different sample sizes. A certified pure Nickel standard sample with 6.3mm diameter was used as a reference for a VSM. During the verification process, Ni foil was cut to 5mm x 5mm square samples to remove shape effect between Ni foil and silicon wafer because of the difficulty in cutting the silicon sample to a round shape. The saturation magnetization of a 5mm x 5mm sample matches reasonably well with the original emu/g value of Ni foil, as shown in Fig. 2.

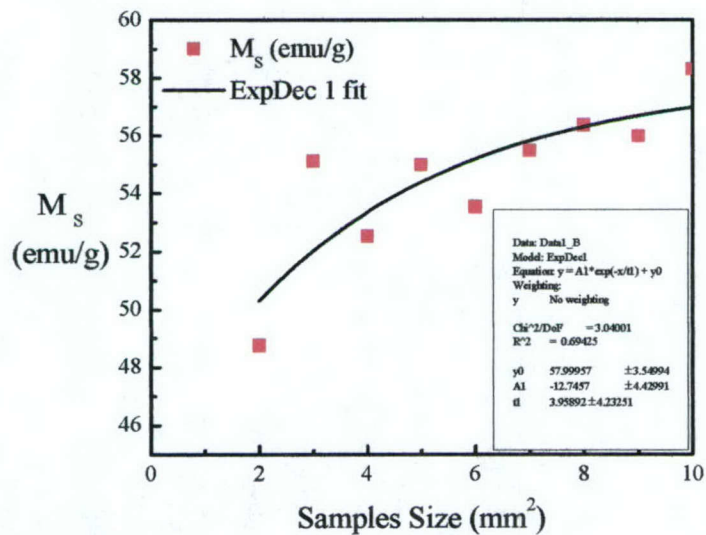


Figure 2. Saturation magnetization of pure Ni foil as a function of samples size.

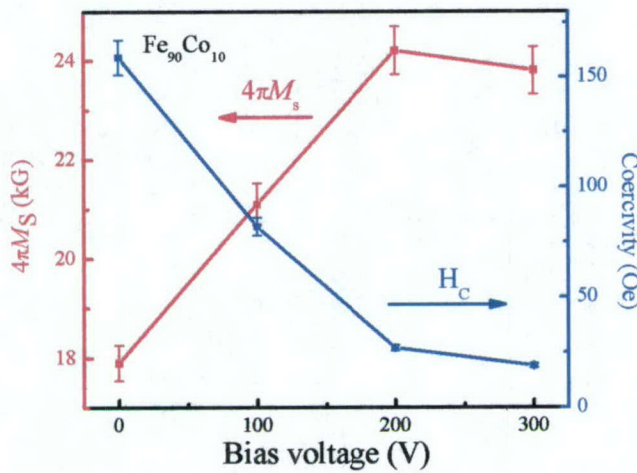


Figure 3. Saturation magnetization and in-plane coercivity of Fe-10%Co films as a function of substrate bias voltage.

Figure 3 shows change of saturation magnetization and in-plane coercivity of Fe-10%Co films as a function of substrate bias voltage. The film thickness was between 180 to 230nm. The saturation magnetization of Fe-10%Co film increased from 17.9 to 24.2 kG with the increase of the substrate bias to 200V, while the coercivity of the film deposited on the silicon decreased to 19 Oe from 159 Oe of unbiased films, as shown in Fig. 3 and Fig. 4. There was no systematic difference in composition between biased and unbiased films from EDX data, and it corresponded to the target composition. XRD patterns showed both biased and unbiased films that have a bcc structure. This property should not be varied as a function of this process because saturation magnetization is one of the intrinsic properties of a material. However, it is clearly shown in the figure that the substrate bias during dc magnetron sputter process significantly influenced the saturation magnetization of Fe-10%Co films.

In order to improve the accuracy of the density measurement, the thickness of Fe-5%Co alloy films is intentionally increased to 1.5 μm . The density of 300 V biased and unbiased film was 7.97 and 7.86 g/cm^3 , respectively, which was very close to the theoretical value of 7.92 g/cm^3 for Fe-5% Co alloy.

TEM microstructures and selected area diffraction (SAD) from 300 V bias and unbiased of Fe-10%Co film are shown in Fig. 5. The 300 V biased film has a well-defined columnar structure which are 20 nm in diameter. However, the unbiased film shows randomly oriented crystallites existing near the interface between the film and substrate. In order to obtain high magnetization of the film, a soft magnetic film requires small grains with good exchange coupling between the grains. Mainly bcc structure is observed in a selected area diffraction pattern from both biased and unbiased films. However, the fcc phase present the unbiased sample rather than 300 V biased one. The fcc phase of pure Fe has $1.39 \mu_B$ compared with $2.2 \mu_B$ of bcc structure [24], so existing fcc phase of Fe can decrease the magnetic moment in the film per unit area. Grain boundary segregation, which is observed from TEM micrographs of 300 V biased film, can be another source of saturation magnetic induction change. The magnetic moment of Fe-Co alloy can be improved by increasing magnetic moment of Fe site to approximately

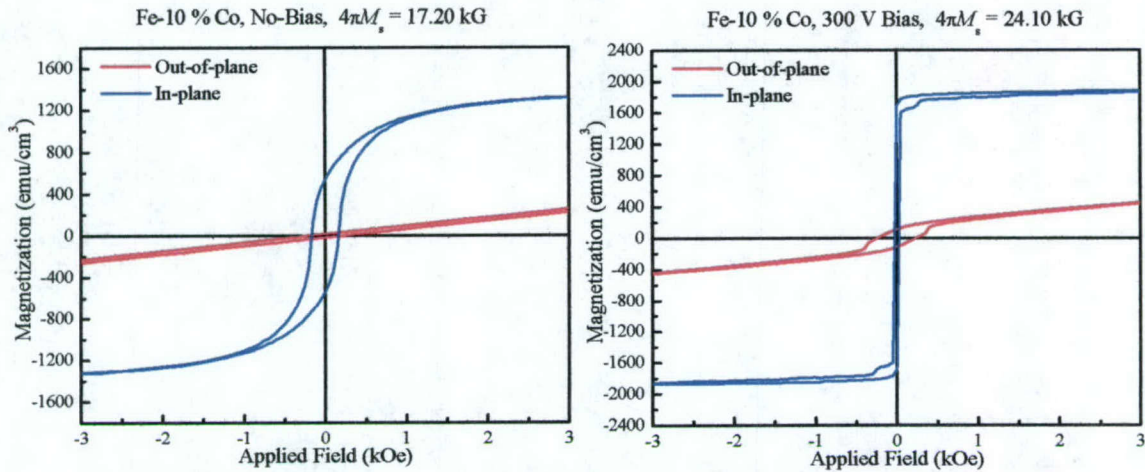


Figure 4. Magnetic properties of Fe-10%Co films as a function of substrate bias voltage.

$3.0 \mu_B$ in ordered CsCl structure from $2.2 \mu_B$ in bcc structured pure Fe [24, 25]. Assuming this segregation has an ordered Fe-Co structure, the average saturation magnetization of a biased film should be increased due to the high moment material at the grain boundaries. The assumption of grain boundary segregation of high moment material is also supported by the sudden jump of an out-of-plane hysteresis loop, which is only observed from biased samples. Those phenomena can be explained by the increase of saturation magnetization of biased films, higher than bulk materials, as shown in Fig. 1, and the magnetostriction of Fe-Co alloy increases with increasing the content of cobalt, followed by a decrease beyond 60 % of cobalt [2]. The magnetostriction (λ) of Fe-10%Co alloy film was 1.89×10^{-5} with 300 V biased, which was very close to the bulk value of 1.89×10^{-5} for Fe-10% Co alloy, as shown in Table 1.

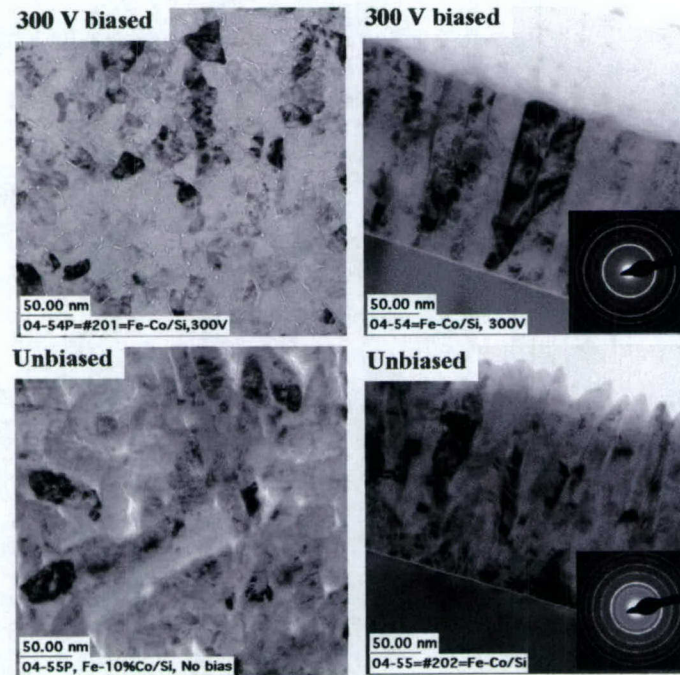


Figure 5. TEM images of biased and unbiased Fe-10%Co thin film.

Table I. Magnetostriction data for Fe-30%Co and Fe-10%Co as a function of bias voltage.

Description	λ (Measured)	λ (R. M. Bozorth)	$4\pi M_s$
Fe ₉₀ Co ₁₀ with 300 V bias	1.92×10^{-5}	N/A	24.13 kG
Fe ₉₀ Co ₁₀ without bias	Hard	1.7×10^{-5}	17.21 kG
Fe ₉₀ Co ₃₀ with 300 V bias	4.41×10^{-5}	N/A	24.32 kG
Fe ₉₀ Co ₃₀ without bias	Hard	4.4×10^{-5}	19.08 kG

The dependence of easy-axis coercivity of Fe-Co films on the thickness of Co seed-layer shown in Fig. 6. Fe-5%Co alloy target was used for the deposition of the film. The bias voltage, dc power density and Ar gas pressure for this specific experiment were 300V, 10W/cm² and 1 mTorr, respectively. The effects of seed-layer on Fe-Co films were thoroughly investigated by Jung *et al.* [8, 9, 26]. A remarkable reduction of in-plane coercivity was found in sputtered Fe₆₅Co₃₅ films, when several different seed-layers, such as Cu, Ta, NiFe, Ru, Ta-NiFe and Ta-Cu were deposited prior to Fe-Co film. Through extensive magnetic and structural characterization of Fe-Co films, they concluded that the decrease of coercivity was correlated to the reduction of grain size. Co seed-layer demonstrated very similar effect on the coercivity of Fe-5%Co alloy thin film. The coercivity decreased from 16.1 to 2.8 Oe, when 2.5nm of Co seed-layer was deposited. However, the coercivity slightly increased with the increase of the seed-layer up to 50nm. In order to further improve soft properties and increase the resistivity of Fe-Co films, Fe-10%Co target with 1% Al₂O₃ was used. With 50 Oe of applied field during the deposition, a commercially available (Fe-10%Co)₉₉(Al₂O₃)₁ alloy 2 inch target was used to grow the films. Figure 7 shows the magnetic property of (Fe-10%Co)₉₉(Al₂O₃)₁ with 50 Oe of applied field during deposition. The anisotropy field (H_k) is observed to be 390 Oe on MgO (111) single crystal substrate using B-H loop tracer. The easy axis coercivity, squareness ratio, and resistivity of this film were 8.8 Oe, 0.99, and 28 $\mu\Omega\text{-cm}$, respectively. Figure 8 shows permeability spectra model [1] based on the magnetic data of (Fe-10%Co)₉₉(Al₂O₃)₁ film. The calculated FMR frequency was

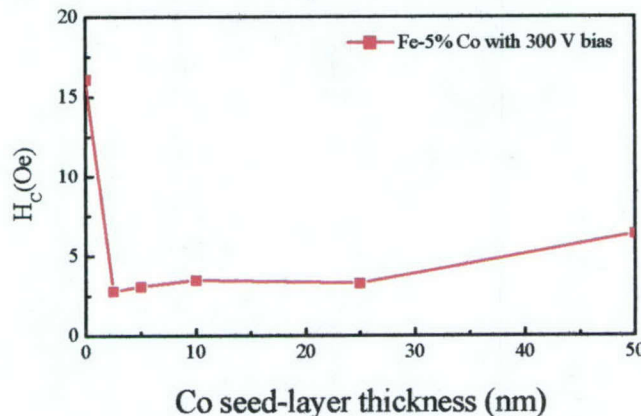


Figure 6. In-plane coercivity for Fe-5%Co thin film as a function of thickness of Co seed-layer

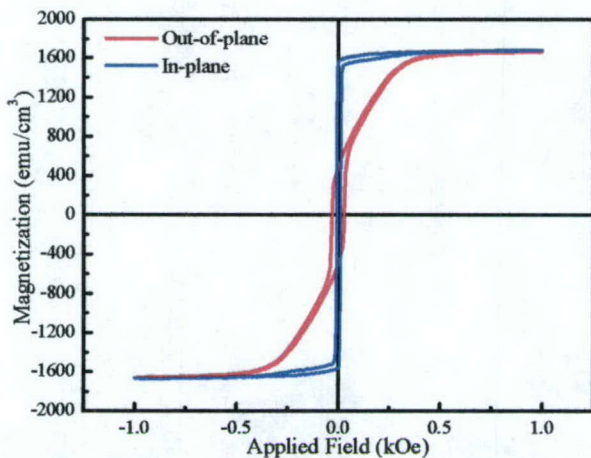


Figure 7. Magnetic properties of 200V biased $(\text{Fe-10\%Co})_{99}(\text{Al}_2\text{O}_3)_1$ thin films with 50 Oe applied field during deposition.

7.9 GHz and operating frequency will be 5.7 GHz with 10 of the quality factor. This magnetic film should be adequate for applications utilizing a thin film inductor over 5 GHz applications.

The final part of this report consists of design and fabrication of thin film inductor. A detailed fabrication step is illustrated in appendix I. Also shown in appendix I is the top view and cross-section of construction diagrams that show how the thin film inductor was made. Figure 9 shows four-turn copper tracer on silicon wafer, which was made using electron beam photolithography process.

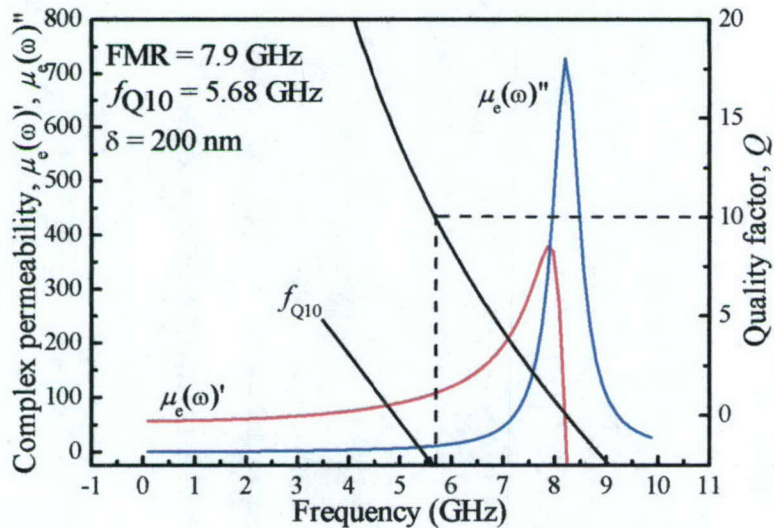


Figure 8. Complex permeability spectra. The parameters are $H_k = 390$ Oe, $4\pi M_s = 22$ kG, $\alpha = 0.01$, and $\rho = 50\Omega\mu\text{cm}$.

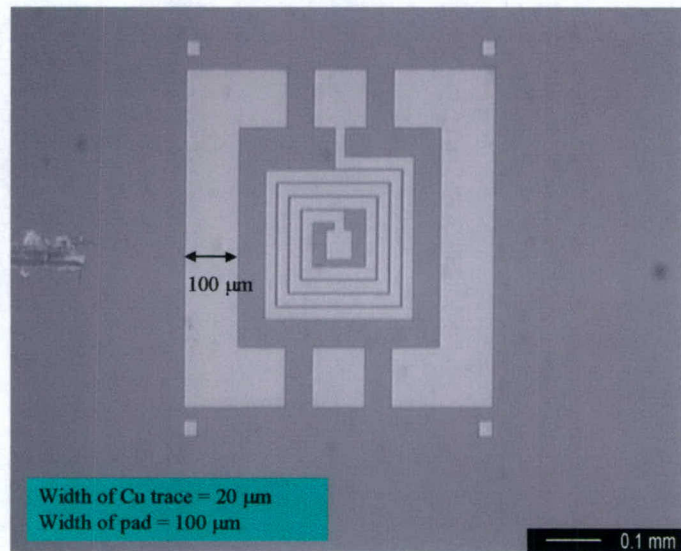


Figure 9. 4 turn copper tracer fabricated using e-beam lithography.

References

1. T. Tanaka, Y.K. Hong, S.H. Gee, M.H. Park, D.W. Erickson, and C. Byun, IEEE Trans., Magn. **40**, 2005 (2004)
2. R. M. Bozorth, *Ferromagnetism*, IEEE press, New York, 1993
3. S. Ikeda, I. Tagawa, Y. Uehara, T. Kubomiya, J. Kane, M. Kakehi and A. Chikajawa, IEEE Trans. Magn., **38**, 2219 (2002)
4. S.X. Wang, N. X. Sun, M. Yamaguchi, and S. Yabukami, Nature (London) **407**, 150 (2000)
5. T. Osaka, M. Takai, K. Hayashi, K. Ohashi, M. Saito, and K. Yamada, Nature (London) **392**, 796 (1998)
6. L.H. Chen, Y. H. Shih, K. A. Ellis, S. Jin, R. B. van Dover, and T. J. Klemmer, IEEE Trans. Magn., **36**, 3418 (2000)
7. N.X. Sun and S.X. Wang, J. Appl. Phys., **92**, 1447 (2002)
8. H. S. Jung and W.D. Doyle, IEEE Trans. Mag., **39**, 679 (2003)
9. H. S. Jung, W. D. Doyle, and S. Matsunuma, J. Appl. Phys., **93**, 6462 (2003)
10. H. Du, G. Pan, and R. Buckley, J. Appl. Phys. **91**, 7827 (2002)
11. W. Yu, J.A. Bain, Y. Peng and D.E. Laughlin, IEEE Trans. Magn. **38**, 3030 (2002)
12. J.A. Thornton, J. Vac. Sci. Technol. **11**, 663 (1974)
13. N.X. Sun, S. X. Wang, T. J. Silva, and A. B. Kos, IEEE Trans. Magn., **38**, 146 (2002)
14. H. Jiang, Y. Chien and Guoda Lian, IEEE Trans. Magn., **39**, 3559 (2003)
15. S. Ohnuma, N. Kobayashi, T. Masumoto, S. Mitani, and H. Fujimori, J. Appl. Phys., **85**, 4574 (1998)
16. K. Shintaku, K. Yamakawa, and K. Ouchi, J. Appl. Phys., **93**, 6474 (2003)
17. N.A. Lesnik, C. J. Oates, G.M. Smith, P.C. Reidi, G.N. Kakazei, A.F. Kravets, and P.E. Wiegen, J. Appl. Phys., **94**, 6631 (2003)
18. R.E. Jones, C.L. Stnadley and L.I. Maissel, J. Appl. Phys., **38** 4656 (1967)

19. S.M. Rossnagel, J.J. Cuomo, and W.D. Westwood, edited, "Handbook of Plasma Processing Technology", Noyes Publications, New Jersey, 1990
20. J.A. Thornton, Thin Solid Films 40, 335 (1977)
21. L.I. Maissel and P.M. P.M. Schaible, J. Appl. Phys., 36, 237 (1965)
22. J.J. Cuomo, J.M.E. Harper, C.R. Guarnieri, D.D. Yee, L.J. Attanasio, C.T. Wu and R.H. Hammond, J. Vac. Sci. Technol. 20, 349 (1982)
23. D.M. Mattox and G.J. Kominik, J. Vac. Sci. Technol., 9, 699 (1971)
24. C.H. Park, I.G. Kim, B.C. Lee and J.I. Lee, Phys. Stat. Sol. (b) 241, 1419 (2004)
25. T.R. McGuire and D.I. Bardos, J. Appl. Phys., 40, 1371 (1969)
26. H. S. Jung, W. D. Doyle, H. Fujiwara, J. E. Wittig, J. F. Al-Sharab, J. Bentley, and N. D. Evans, J. Appl. Phys., 91, 6899 (2002)

IV. Accomplishments

1. Publications

(a) Papers in referred journals (authors; title; journal; volume, page, (year)):
 T. Tanaka, Y.K. Hong, S.H. Gee, M.H. Park, D.W. Erickson, and C. Byun, IEEE Trans., Magn. 40, 2005 (2004)

(b) Books or Book chapters: None

2. Patents:

3. Presentations (invited - contributed):

1. T. Tanaka, Y. K. Hong, M. H. Park, S. H. Gee, D. W. Erickson, "An expectation of a 3-GHz-band thin film inductor," 17aC-11, 27th annual conference on magnetic in Japan, Osaka, Japan, September 2003.
2. T. Tanaka, Y. Hong, M. Park, S. Gee, and D. W. Erickson, "Estimation of soft magnetic film properties to meet a 3-GHz-band thin film inductor," AQ-08, 9th Joint Magnetism and Magnetic Materials/Intermag conference, Anaheim, California, January 2004.
3. C. Byun, Y. K. Hong, M. H. Park, S. H. Gee, and M. Kim, "Effects of substrate bias on saturation magnetization and soft magnetic properties of Fe-10% Co alloy thin film," ED-03, 49th Annual Conference on Magnetism and Magnetic Materials, Jacksonville, Florida, November 2004

4. Honors

5. Number of graduate students supported: 1
 Number of Post-doctoral students involved: 1
 Number of undergraduate students supported: 2
 Number of under-represented members by group: 0

Appendix I. Fabrication steps of thin film inductor

Chip Inductor wafer process

Substrate	Thermally oxidized Silicon wafer (100 or 111)	
Size	3" flat*	* AJA sputtering system can handle only 3" wafers
Step	Process	Equipment
100	Cleaning of 3" wafer*	
200	Deposit 1st insulation layer	
	Deposit 1st insulation layer	SiO2
		AJA
Mask #1	Deposit 1st magnetic layer	
300	Deposit seedlayer*	AJA
310	Deposit magnetic layer*	AJA
320	Measure properties*	
330	Spin coat of PR*	AZ 4000
340	Mask/expose	
350	Post exposure bake of PR	110 C
360	Develop	
370	Etch 1st magnetic layer	
380	Inspection	
Mask #2	Deposit 2nd insulation layer	
400	Deposit 2nd insulation layer*	SiO2
410	Measure thickness	Dektak
420	Spin coat of PR*	AZ 4000?
430	Mask/expose	
440	Post exposure bake of PR	110 C
450	Develop	
460	Wet etch	
470	Inspection	
Mask #3	Coil deposition	
500	Deposit adhesion layer	100 A of Ti
510	Deposit seedlayer	2000 A of Cu
520	Spin coat of PR*	AZ 4000
530	Mask/expose	5 to 10 micron?
535	Post exposure bake of PR	110C
540	Develop	
550	Electroplating of coil	Cu
560	Descum	Plating bath
570	PR removal	
580	Seed etch	
590	Inspection	Optical microscope

	Planarization		
600	Planarization	Polyimide/HBPR?	Spin coater?
610	CMP		CMP
Mask #4	Deposit 3rd insulation layer		
700	Deposit 3rd insulation layer*	SiO2	AJA
710	Spin coat of PR*	AZ 4000	5 to10 micron?
720	Mask/expose		
730	Post exposure bake of PR	110 C	
740	Develop		
750	Etch 3rd insulation		
760	Inspection		
Mask #5	Deposit 2nd magnetic layer		
800	Spin coat of PR*	AZ4000	
810	Mask/expose		
820	Post exposure bake of PR	110 C	
830	Develop		
840	Deposit seedlayer*		AJA
850	Deposit magnetic layer*		AJA
860	Measure properties*		
870	PR removal		
Mask #6	Deposit 4th insulation layer		
900	Deposit 4th insulation layer*	SiO2	AJA
910	Spin coat of PR*	AZ 4000	5 to10 micron?
920	Mask/expose		
930	Post exposure bake of PR	110 C	
940	Develop		
950	Etch 4th insulation layer		
960	Descum		
970	Inspection		
Mask #7	Deposit thru-via/ground		
1000	Deposit thru-via layer		AJA
1010	Spin coat of PR*	AZ 4000	
1020	Mask/expose		
1030	Post exposure bake of PR	110 C	
1040	Develop		
1050	Etch thru-via		
1060	Descum		
1070	PR removal		
1200	Electrical test		

Development and Characterization of High Resistive Fe-M-O (M=Hf, Zr or rare-earth metals) Soft Magnetic Thin Films

You Qiang,
Physics Department, University of Idaho

I. Abstract

We report here the room-temperature synthesis of Fe/FeO core-shell nanoclusters using our novel nanocluster deposition system, based on the combination of high pressure sputtering with aggregation. Fe/FeO core-shell nanoclusters are of great interest due to its potential application for soft magnetic thin films of inductors. These oxide shells act as passivation layers preventing further oxidation of the cores upon continued exposure to oxygen, and also provide high resistivity. The Fe core reminds the soft magnetic behaviors. We used SEM, HRTEM, XRD and XPS measurements for characterizing nanoclusters and nanocluster films. Magnetic properties of clusters and cluster films have been investigated by SQUID.

II. Approach and Results

A: Approach of Monodispersive Nanoclusters and Nanocluster Films

In the last few years interest in magnetic clusters has grown enormously with increasing attention devoted to the effect of nano-size confinement on the physical properties and with regard to their potential in the nanoscale engineering of materials with very specific properties. The unprecedented ability to assemble nanoclusters into new materials with unique or improved properties is thus creating a revolution in our ability to engineer condensed matter for desired applications.

We have developed a new kind of cluster beam source that combines improved magnetron sputtering with a gas aggregation tube, so called *sputtering-gas-aggregation* source as discussed in [6-13]. This cluster source can produce a very large range of mean cluster sizes (1 to 100 nm), and has a high degree of ionization, from 20% to 50%, depending on the target materials. The sputter discharge ejects atoms and ions into the rare-gas flux, where they aggregate through low-temperature condensation when their density is high enough. The clusters are charged by energetic particles in the plasma, so that no additional electron impact is necessary. This cluster source can produce monodispersed nanoclusters with very narrow size distribution because the heterogeneous growth processes happen in the plasma close to the surface of the target. The mean size of clusters can be easily varied by adjusting the aggregation distance L, the sputter power P, the pressure p in the aggregation tube, and the ratio of He to Ar gas flow rate. The aggregation distance and the ratio of He to Ar gas-flow rate are important parameters for getting a high intensity and low dispersion of the cluster beam.

A major advantage of this type of system is that the clusters have much smaller size dispersion than grains obtained in any typical vapor deposition system. The main features of our new “cluster deposition system” (CDS) are briefly described as follows. Figure 1 shows a photo of the CDS. A cluster source with a 3-inch high-pressure

magnetron-sputtering gun will provide a relatively high intensity cluster beam of deposition rate about 5 A/s. A new high-transmission infinite-range mass selector has been designed for the cluster beam. The mass selector can make the cluster size distribution very narrow of below 5%. A cluster-beam source is combined with atom beams from standard magnetron sputtering sources near the substrate. This technique was used to deposit simultaneously or alternately mesoscopic thin films or multilayers, and offers the possibility to control independently the incident cluster size and concentration. A load-lock chamber attached to the deposition chamber is provided for rapid substrate change. Clearly, this new nanofabrication system provides great opportunity for controlling the magnetic properties of films, and thus facilitates the “nanomaterials-by-design” concept.

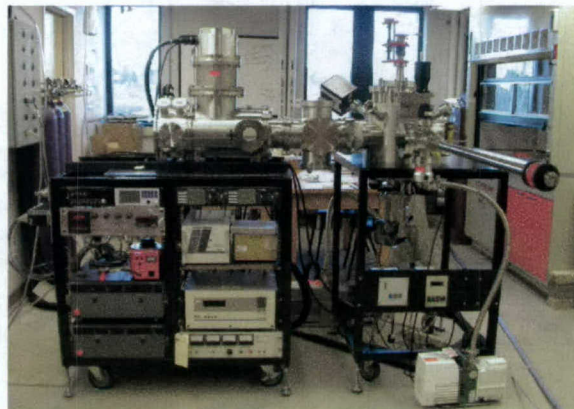


Fig. 1: Cluster deposition system

When oxygen gas is introduced into the deposition chamber during processing, uniform metal oxide shells covering the clusters are formed. For a constant flow of Ar gas, the gas pressure in the deposition chamber can be adjusted by changing the flow rate of oxygen gas (O_2). We have observed that the oxide shell thickness of the clusters is sensitive and controllable to the deposition time and amount of O_2 .

Fe-FeO cluster films with 2 micrometer in thickness has been deposited onto glass or Si substrates in a mixed atmosphere of pure argon and oxygen. The composition of films is controlled in changing the number of pellets of M elements laced onto a pure-Fe or Fe-M alloy targets. By changing the oxygen flow ratios in the deposition chamber, we can control the resistivity of the thickness of shell structures. The films will be subjected to annealing in a glove box for about 10 ks at various temperatures in an evacuated atmosphere below 1023 Pa.

B: Results of clusters and soft magnetic cluster films

- Novel core-shell monodispersive iron-iron oxides nanoclusters with mean sizes varying between 2 to 100 nm, see the Fig. 2. Electron diffraction patterns clearly indicate the coexistence of Fe and iron oxide phases, while the high-resolution TEM images show the Fe clusters to be covered with iron oxides.

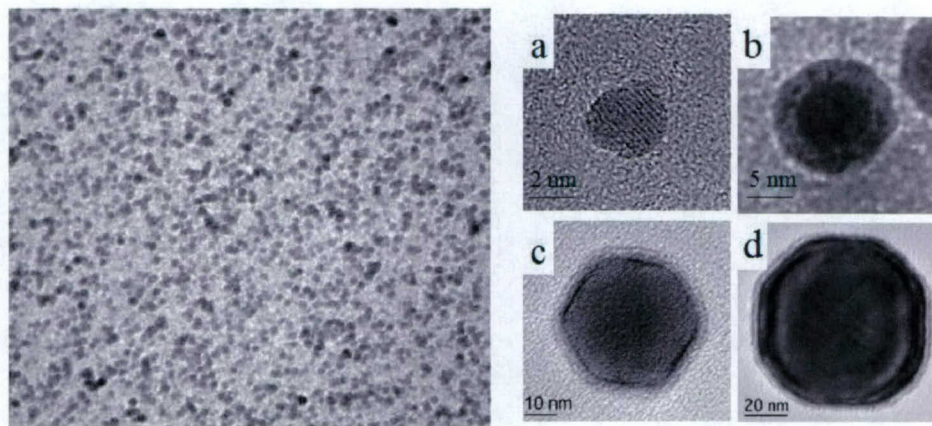


Fig. 2: uniform Fe core-shell nanoclusters

- Nanocluster thin films deposited by using clusters as building blocks (Fig. 3)

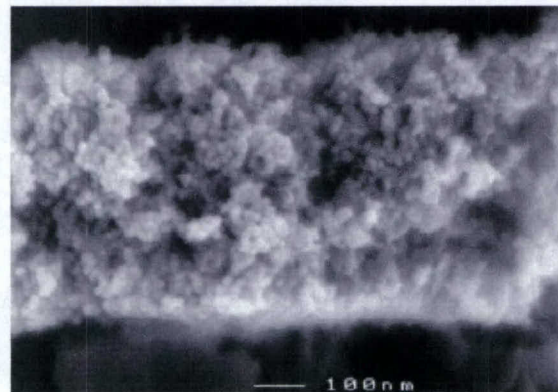


Fig. 3: Nanocluster films

- Soft magnetic nanocomposites of Fe nanoclusters embedded in Co matrix (fig.4)

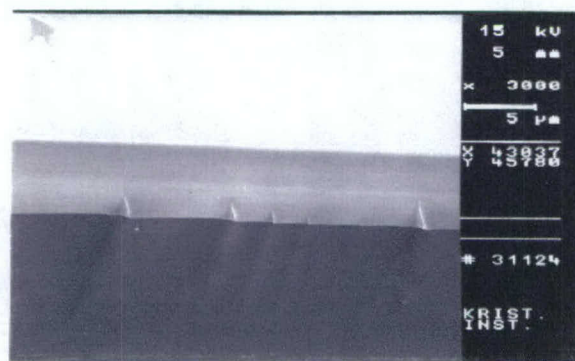


Fig. 4: Fe nanoclusters embedded in Co matrix with thickness about 5 micrometers.

- XRD measurements on nanoclusters

XRD measurements are done using “Philips X’pert MPD System (PW3040/00 type)”. This system is equipped with a fixed, long-fine-focus (Cu) anode with an incident beam angle of 2.50° with a scan axis 2Theta (15° - 85°) for 4 hours. The background subtracted XRD pattern of core-shell Fe/FeO nanocluster thin film is shown in Figure 4. Zero-valent Fe in the sample is detected along with the presence of iron oxide. XRD analysis detected this oxide to be magnetite or maghemite or else a combination of both. The average crystallite size is determined using Scherer equation and is about 7nm for iron and about 3nm for magnetite and/or maghemite. If the clusters are deposited for longer time, and the film is finally exposed to atmosphere, the intensity of Fe^0 peak is found to increase prominently.

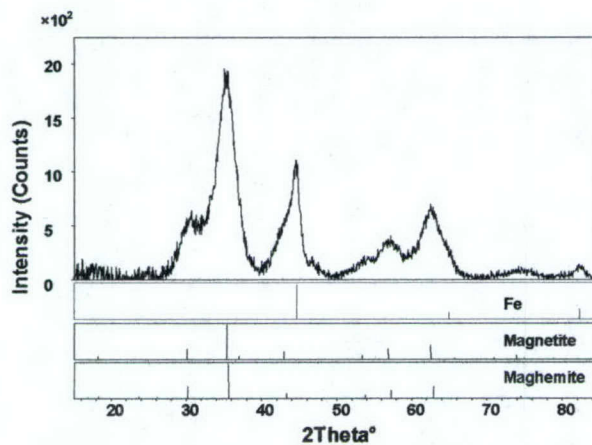


Fig. 5: XRD measurement of iron-iron oxide cluster films.

- Measured magnetic properties of the films by SQUID,

We have measured the magnetic properties of Fe clusters embedded in Co matrix using co-deposition technique. As deposited thin films H_c is about 30 Oe with magnetic moment of 3.5×10^{-3} emu of the sample. When the sample was annealed at 450°C for 30 mins, the coercivity (H_c) became 9.2 Oe and magnetic moment increased up to 7.6×10^{-3} emu. The thin film became much magnetic soft (Fig.6) and almost doubled magnetic moments properly due to FeCo alloying effect.

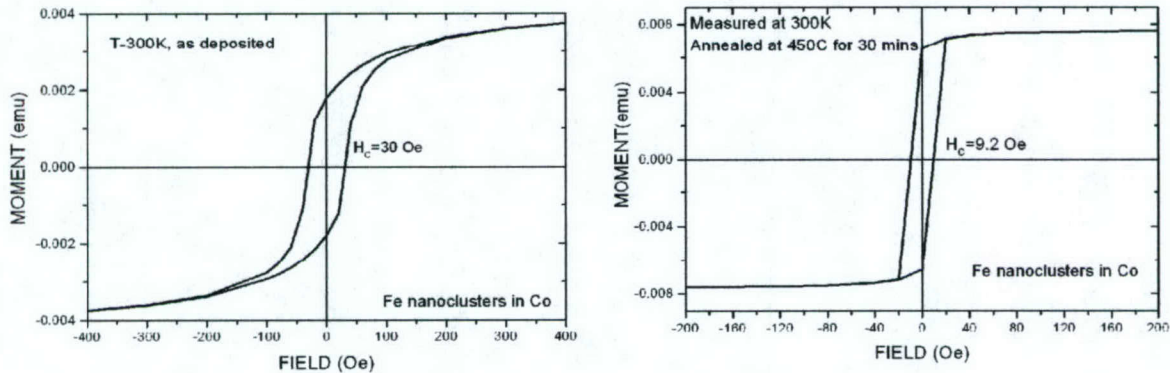


Fig. 6: Magnetic loops of Fe nanoclusters of 3 nm diameter embedded in Co film. Concentration of Fe is about 30%

III. Conclusions

In summary, we successfully prepared stable Fe/FeO core-shell nanoclusters by a technique that is a combination of sputtering and aggregation. SEM, HRTEM, XRD and analysis are done on this sample and all of these measurements confirmed the presence of metallic Fe core and its oxide shell. Magnetic moments have been enhanced by annealing the cluster film of Fe clusters embedded in a Co matrix, and the magnetic softness of the film also increased.

We recommend future studies on the quantitative relationship between cluster size and oxygen concentrations and the magnetic properties. This will lead to a greater understanding of the relative importance of nanoparticle size mechanism to success of our highly effective process for achievement of the desired goals.

References

1. Y. Hayakawa, A. Makino, H. Fujimori and A. Inoue, "High resistive nanocrystalline Fe-M-O (M=Hf, Zr, rare-earth metals) soft magnetic films for high-frequency applications", *J. Appl. Phys.* 81 (8), 3747 (1997); *Nanostruct. Mater.* 6, 989 (1995)
2. P. Pieters, et. al. "Accurate Modeling of High-Q spiral inductors in thin-film multiplayer technology for wireless telecommunication applications", *IEEE trans. on microwave and techniques*, 49, 4 (2001), p589
3. M. A. Willard, et. al., "Structure and Magnetic Properties of (Fe0.5 Co0.5)88Zr7B4Cu1 nanocrystalline alloys", *J. Appl. Phys.*, 84, 12 (1998)6773
4. M.A. Willard, et. al., "Structure and Magnetic properties of (Co, Fe)-based nanocrystalline soft magnetic materials", *J. Appl. Phys.*, 91, 10 (2002)8420
5. G. Herzer, *IEEE Trans. Magn. Magn.* 25, 3327 (1989). *IEEE Trans. Magn. Magn.* 26, 1397 (1990).
6. H. Haberland, M. Mall. M. Moseler, Y. Qiang, Th. Reiners and Y. Thurner, "Filling of Micron-sized Contact Holes with Copper by Energetic Cluster Impact," *J. Vac. Sci. Technol. A12* 2925 (1994)
7. H. Haberland M. Moseler, Y. Qiang, Th. Reiners and T. Thurner, "Energetic Cluster Impact (ECI): a New Method for Thin Film Formation," *Surf. Rev. Lett.* 3 887 (1996)

8. H. Haberland, M. Leber, M. Moseler, Y. Qiang, *et al.*, "A New Low Temperature Thin Film Deposition Process: Energetic Cluster Impact (ECI)," *Mat. Res. Symp. Proc.* **338** 207 (1996)
9. Y. Qiang, Y. Thurner, Th. Reiners, O. Rattunde and H. Haberland, "Hard Coatings (TiN, $Ti_xAl_{1-x}N$) Deposited at Room Temperature by Energetic Cluster Impact," *Surf. Coat. Technol.* **27** 100 (1998)
10. Y. Qiang, R. Morel, D. Eastham, J.M. Meldrim, J. Kraft, A. Fert, H. Haberland, D.J. Sellmyer, "Magnetic Properties of Cobalt Clusters Embedded in a Nonmagnetic Matrix (Ag, Cu, and SiO₂), in *Cluster and Nanostructure Interfaces*, eds., P. Jena, S.N. Khanna, B.K. Rao World Scientific, Singapore (2000), p. 217
11. D.J. Sellmyer, C.P. Luo, Y. Qiang, J.P. Liu, "Magnetism of Nanophase Composite Films," in *Handbook of Thin Film Materials*, Vol. 5, ed. H.S. Nalwa, Academic Press (2002), pp. 5, 337
12. J.M. Meldrim, Y. Qiang, D.J. Sellmyer, H. Haberland, "Magnetic properties of cluster-beam synthesized Co-noble metal films", *J. Appl. Phys.* **87** 7013 (2000)
13. Y. Qiang, R.F. Sabiryanov, S.S. Jaswal, H. Haberland and D.J. Sellmyer, "Magnetism of Monodispersed Co Nanocluster Films", *Phys. Rev. B* **66** 064404 (2002)
14. Y. Qiang, Y. Xu, Z. Sun, J. Long and D.J. Sellmyer, "Synthesis and Magnetic Properties of L₁0 – CoPt Nanocluster Films", *Proc. 47th Conf. Magnetism and Magnetic Materials*, Nov. 11 – 15, Tampa, FL, to be published in *J. Appl. Phys.*
15. K.-H. Meiwes-Broer, "Metal Clusters at Surfaces", Springer (2001)
16. P. Milani and S. Iannotta, "Cluster Beam Synthesis of Nanostructured Materials", Springer (2001)
17. P. Moriarty, "Nanostructured Materials", *Rep. Prog. Phys.* **64** 297 (2001)
18. C. Binns, "Nanoclusters Deposited on Surfaces", *Surf. Sci. Rep.* **44** 1 (2001)

IV. Accomplishments

1. Publications:

1. **Y. Qiang**, J. Antony, M. G. Marino, and S. Pendyala, "Synthesis of Core-Shell nanoclusters with High Magnetic Moment for Biomedical Applications", *IEEE Transactions on Magnetics*, **40**, 3538 (2004)
2. J. Antony, X.B. Chen, J. Morrison, L. Bergman, **Y. Qiang**, D.E. McCready, and M. Engelhard, "Sythesis and Optical Properties of ZnO nanoclusters", *Appl. Phys. Letters*, submitted, Oct. 04
3. J. Antony, S. Pendyala, A. Sharma, X.B. Chen, J. Morrison, L. Bergman, **Y. Qiang**, "Room temperature ferromagnetic and UV optical properties of Co-doped ZnO nanocluster films", *J. of Appl. Phys. in press*, 2005

2. Presentations (contributed):

Conference Contributions:

- 1) Y. Qiang, J. Antony, M. G. Marino, and S. Pendyala, "Synthesis of Core-Shell Nanoclusters with High Magnetic Moment for Biomedical Applications", 9th joint MMM/INTERMAG Conference, Anaheim, Cal. Jan. 5-9, 2004.

- 2) D. Baer, J. Antony, K. Pecher, Y. Qiang, et. al., "Characterization and Properties of Iron and Iron-Oxide Nanoparticles", the 227th ACS National Meeting, Anaheim, CA, March 28-April 1, 2004 in Anaheim, California.
- 3) J. Antony, S. Pendyala, A.S. Shenoy and Y. Qiang, "Magnetism of size and shape controlled core-shell nanoparticles", APS March Meeting, Montreal, Canada, March 22-26, 2004.
- 4) J. Antony, X.B. Chen, L. Bergman and Y. Qiang, "Synthesis and optical properties of ZnO nanoclusters", APS March Meeting, Montreal, Canada, March 22-26, 2004.
- 5) Jiji Antony, You Qiang, Don Baer, C.M. Wang, David E McCready and H. Engelhard, "Synthesis of Iron –Iron oxide Core-shell nanoclusters for Environmental Applications", NW-APS meeting, May 21-22, 2004, Moscow, ID-Pullman, WA
- 6) Jiji Antony, You Qiang, X.B. Chen, L. Bergman, David E McCready and H. Engelhard, "Synthesis and optic properties of ZnO nanoclusters", NW-APS meeting, May 21-22, 2004, Moscow, ID-Pullman, WA
- 7) D. Baer, J. Antony, K. Pecher, Y. Qiang, et. al., "Physical and Chemical Properties of Iron and Iron-Oxide Nanoparticles", the AVS 51st International Symposium, November 14 - 19, 2004 in Anaheim, CA, USA.
- 8) You Qiang, Jiji Antony, Donald R. Baer, Sweta Pendyala and Chongmin Wang, "Synthesis and Applications of Oxide Nanoclusters and Nanocluster-Assembled Materials", 41st Annual Meeting of The Clay Minerals Society (CMS), Richland, WA, 6/23/04
- 9) You Qiang, Jiji Antony, Amit Sharma, Sweta Pendyala, Joe Nutting, Daniel Meyer and Daniel Sikes, "Nanocomposites made out of nanoclusters as building blocks for space applications", MRS04 Fall, Boston.

Invited Talks:

- 1) Y. Qiang, "Nanoclusters and Nanocluster-Assembled Materials-a new way to make nanocomposites", Tenth Annual International Conference on Composites/Nano Engineering (ICCE-10), New Orleans, Louisiana, US, July 20-26, 2003
- 2) Y. Qiang, "Controllable Nanostructured Materials Made out of Nanocluster Building Blocks", Department of Physics, Washington State University, Nov. 11, 2003.
- 3) Y. Qiang, "Nanocluster Films with Controllable Nanostructures", Nanoscale Physics and Devices Laboratory, Institute of Physics, Chinese Academy of Science, Dec. 18, 2003.
- 4) Y. Qiang, "Magnetism: from Free Clusters to Cluster Assembled Materials", Magnetism and Magnetic Materials Division, Shenyang National Laboratory for Materials Science, China. 12-23-2003,
- 5) Y. Qiang, "A Big Challenge: from Free Clusters to Cluster Assembled Nanomaterials", Department of Physics, & National Laboratory of Solid State Microstructures, Nanjing University, China, 12-25-2003.
- 6) Y. Qiang, "Mass Selection, Deposition and Magnetism of Nanoclusters", supported by NITECH 21st Century COE Programme on Environment Friendly Ceramics, Nano-functional Materials Laboratory, Department of Urban Planning and Environment Technology & Department of Materials Science and Engineering. Nagoya Institute of Technology, Japan, Jan. 9-13, 2004.
- 7) Y. Qiang, "Nanomaterials Made Out of Cluster Building Blocks: *Synthesis, Magnetism and Applications*", invited lecture of UW MSE 498/ WSU MSE 599 Jan. 5 to Jan. 23, 2004

- 8) You Qiang, Jiji Antony, Donald R. Baer, Sweta Pendyala and Chongmin Wang, "Synthesis and Applications of Oxide Nanoclusters and Nanocluster-Assembled Materials", 41st Annual Meeting of The Clay Minerals Society (CMS), Richland, WA, 6/23/04
- 9) You Qiang. "Nanomagnetism in nanocluster-assembled materials", Physics Department, Georgia Institute of Technology, Atlanta, November 3, 2004
- 10) You Qiang, Jiji Antony, Amit Sharma, Sweta Pendyala, Joe Nutting, Daniel Meyer and Daniel Sikes, "Nanocomposites made out of nanoclusters as building blocks for space applications", MRS Fall meeting in Boston, November 29-December 3, 2004.

3. Number of graduate students supported: 1
Number of undergraduate students supported: 3

Low-Temperature Chemical Growth of High Magnetization-High Permeability Ferrite Films

D. Eric Aston
Department of Chemical Engineering

I. Abstract

Aqueous spin-spray plating for soft magnetic ferrite film deposition onto silicon substrates has been designed and implemented. The temperature dependence of the growth and magnetic properties these films has been investigated, particularly near the "ferrite formation threshold" of 90°C. Deposition temperature and ion concentrations were varied to determine the optimum synthesis desired magnetic properties of low coercivity, high permeability, and high magnetization, measured with vibrating sample magnetometry (VSM). Surface roughness and film thickness were analyzed with atomic force microscopy (AFM). Recommendations for improvements to the current system design and film production quality are included to fine-tune the process for inductor chip manufacturing. Langmuir-Blodgett (LB) deposition of colloidal multilayers has also been pursued for depositing magnetic materials with pre-existing magnetic properties.

II. Approach and Results

A schematic of the spin-spray deposition system design for depositing soft magnetic ferrite films is shown in Fig. 1. Divalent metal ions (from FeCl_2 , ferrous chloride, and NiCl_2 , nickelous chloride) are dissolved in de-ionized and distilled water for spraying separately from the oxidizer. The oxidizing solution of sodium nitrite (NaNO_2) is buffered to pH 6.9-7 with ammonium acetate ($\text{CH}_3\text{COONH}_4$), also de-ionized and distilled water. Our spray flow rates of 9 ml/min are much lower than previously reported,^{1,2} which is a great improvement in process efficiency.

Our experiments showed that the spraying and reactive coating process must be accomplished free of ambient oxygen, either in from the air or dissolved in solution. The entire substrate and heater assembly was enclosed by a plexi-glass box purged with nitrogen, which eliminates undesirable side reactions.³ The solutions were de-oxygenation by purging with a nitrogen bubbler immediately before deposition. The stage rotating at 150 rpm is heated to steady-state temperature while spraying de-ionized water to eliminate transient thermal effects to the film deposition. The surface temperature is measured directly with an infrared pyrometer, and the water spray is switched to the reactant solutions upon reaching steady state.

A series of samples were made at temperatures varying from 70 to 165°C using solution concentrations of 3 g/l FeCl_2 and 1.5 g/l NiCl_2 in order to investigate the significance of the reported nickel ferrite formation threshold temperature of 90°C.² (Substrate temperatures above the boiling point of the solutions are possible under steady-state spraying due to heat transfer rate limits.) As seen in Fig. 2, above 102°C there appears to be a linear increase in saturation magnetization (M_s) as the deposition

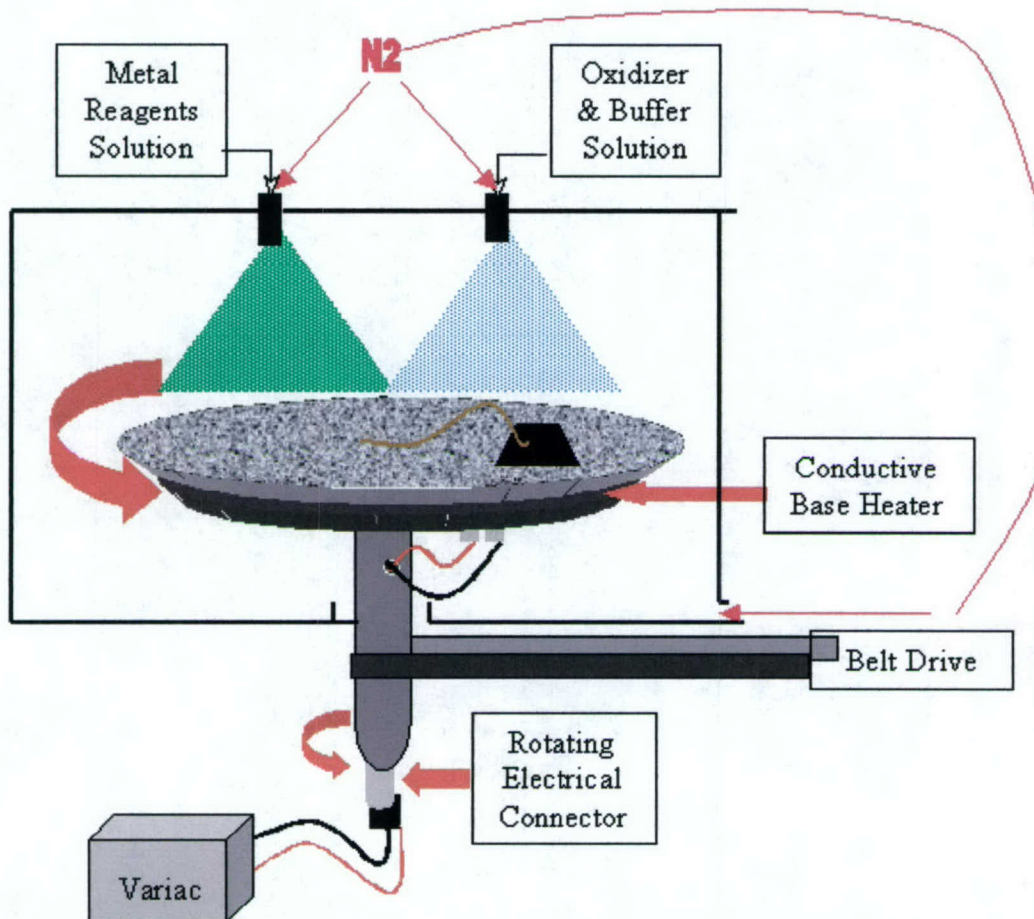


Figure 1: A 20-mm square of test grade semiconductor silicon is attached via a spring clip to a 10 cm OD, 4 cm ID rotating ring heater (1 KW max. output). A three-phase controlled AC drive allows variable substrate rotation of 25 to 1000 rpm. The motor is coupled with 2:1 reduction timing pulleys and belt. A rotating electrical connector allows fixed connection of the heater. Two reactant solutions are fed through atomizing nozzles with nitrogen gas propellant. The nozzles are located 4-12 cm above and normal to the substrate, impinging on opposite halves of the spinning stage. The rotation platform facilitates faster removal of excess water, buffer, reactants, and reaction bi-products (such as Cl^-).

surface temperature decreases, or approaches the threshold. Below 85°C this trend is clearly discontinued and the saturation magnetization drops by a factor of 3-4.

Figure 2 also shows a nearly linear decrease in coercivity (H_c) for the temperature range above 102°C. The process remains difficult to control in the range of 85-102°C due to the delicate balance of a completely wetted substrate under rapid evaporation. Higher temperatures allow stable growth, but the resultant films are very rough and with irregular adhesion. Films deposited at 85°C and cooler are very smooth and possessed very high adhesion to the substrate. Atomic force microscopy (AFM) measurements of surface roughness and film thickness yield much more accurate and small area scale RMS surface roughness values than scanning electron microscopy or ellipsometry, respectively. A scratch made with a steel razor blade allows for accurate thickness measurements of the films. For example, one film made at 70°C with 30 minutes of deposition had an average thickness of 911 nm (30 nm/min). This is comparable to other reports of spin-spray ferrite plating for much higher flow rates, demonstrating that the actual reaction deposition rate is temperature limited, not transport limited.

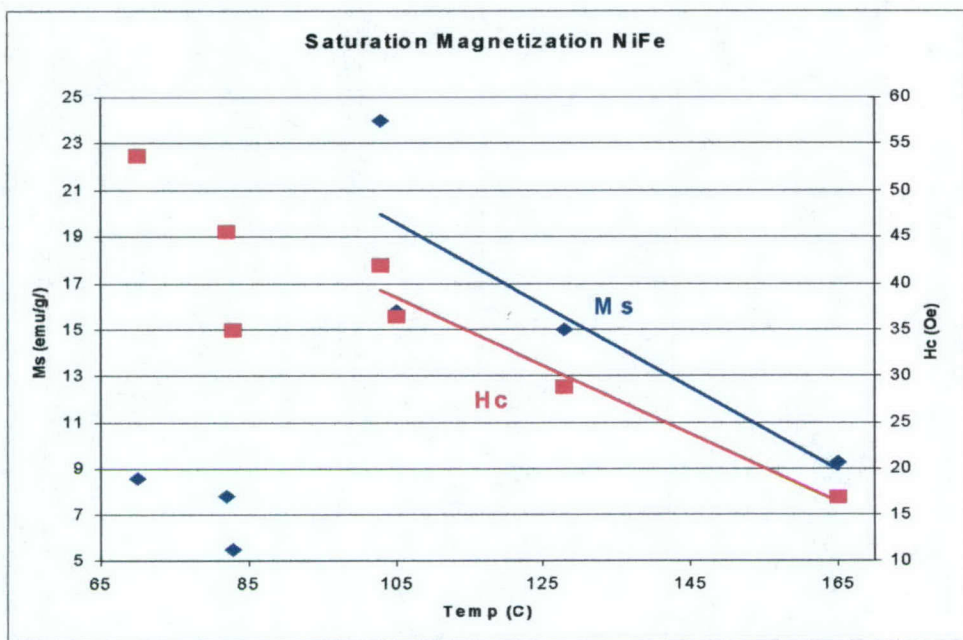


Figure 2: The saturation magnetization (Ms) and coercivity (Hc) is shown as a function of nominal deposition surface temperature for metal solutions containing 3 g/l FeCl_2 and 1.5 g/l NiCl_2 hydrates.

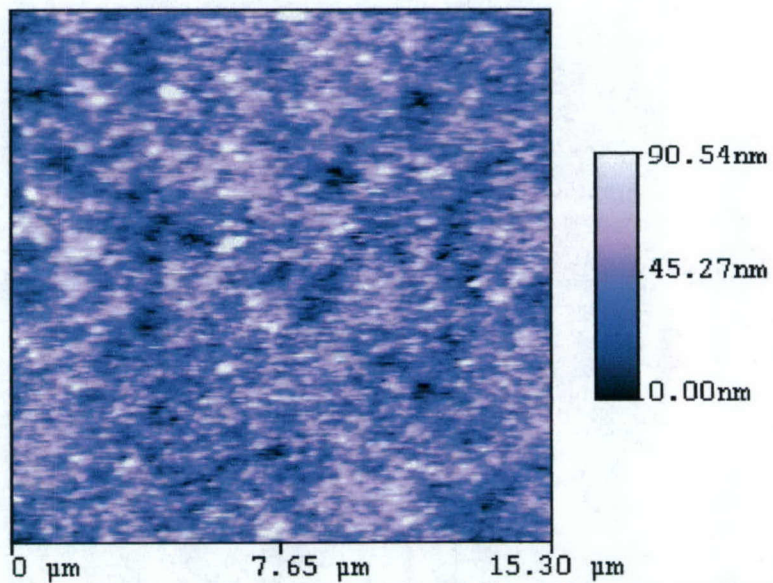


Figure 3: Atomic force micrograph of spin-spray ferrite film: 17 nm rms roughness.

AFM analysis showed an RMS surface roughness of 17 nm (Fig. 3). This is difficult to compare to other reports for grain size, which is not a true measurement

they tend to use SEM to depict an average of surface roughness.

In addition to analyzing the temperature dependence for nickel ferrite films, we completed several other experiments on magnetite (iron ferrite) formation dependence on Fe^{3+} concentration in solution, by adding FeCl_3 . When nickel is not included in the spraying solution, we find the temperature effect on the resultant film magnetization is reversed (Fig. 4). That is, for magnetite formation, higher deposition surface

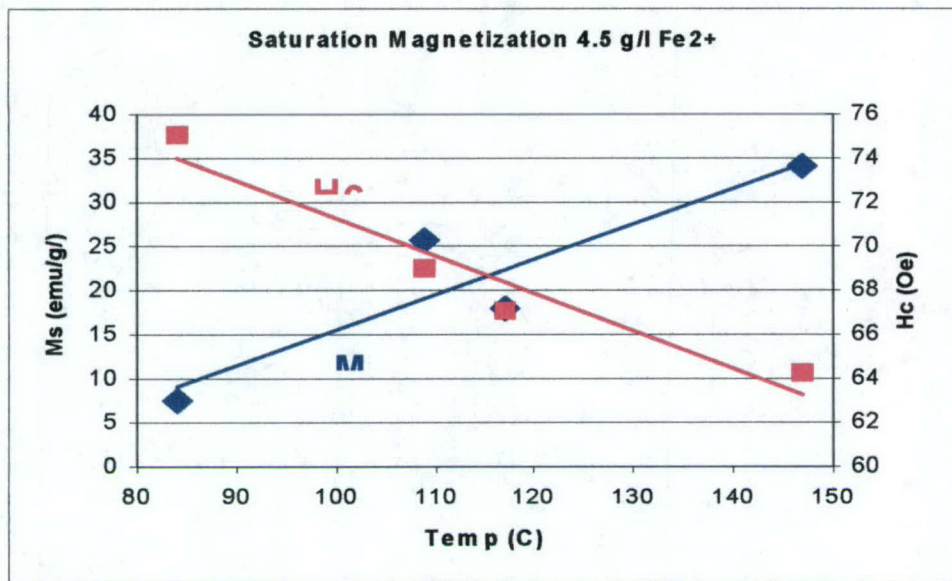


Figure 4: The saturation magnetization (M_s , diamonds) and coercivity (H_c , squares) are shown as functions of nominal deposition surface temperature for metal solutions containing 34.5 g/l FeCl_2 and no NiCl_2 hydrates.

temperatures result in increased saturation magnetization. The coercivity still follows the decreasing trend with temperature as for the nickel ferrite, though less pronounced.

Many samples were made that gave saturation magnetization values over 20 emu/g, comparable to commercially available nickel ferrite powders (e.g., 32 emu/g). The highest M_s obtained by spin-spraying was for magnetite (i.e., no nickel) at 34.2 emu/g. The lowest coercivity obtained was 33.4 Oe for a sample produced with 9:1 mix of $\text{Fe}^{2+}:\text{Fe}^{3+}$ ions at 117°C, compared to 1.6 Oe for the commercial magnetite powders. Our iron ferrites are comparable to nickel ferrites made by this same procedure.⁴

Langmuir Blodgett (LB) deposition of magnetic colloids was investigated as an alternative to spin-spray plating. Pre-existing nickel ferrite powders were suspended in stearic acid, hexanes, chloroform, or a mixture of these for dispersion into monolayers that can be organized into close-packed arrays for layer-by-layer deposition. Silicon substrates were dipped into the prepared LB films and multilayers were deposited at constant surface pressure to maintain constant particle packing. A single film takes as long as hours or days to complete, dependent on the surface area and number of layers deposited. The resultant film roughness of 200 layers was approximately 150 nm rms, much larger than expected for close-packed primary colloids (\varnothing 20-40 nm). Smaller magnetic clusters and/or increased monodispersity will facilitate smooth film deposition.

III. Conclusions

We have detailed the temperature dependence for the formation of nickel ferrite using the spin spray method, which has not been previously reported. We have successfully prepared magnetic films with saturation magnetization that exceeds common commercial nickel ferrite powders, and still have coercivity comparable to previously published data for films made by spin-spray.

While significant progress has been made toward developing this low-temperature chemical process, there are a few additional steps that will improve both the magnetic

and film properties of the samples, as well as the ease of deposition and quality control. We have shown that the extreme temperature-sensitivity of nickel ferrite formation on saturation magnetization requires exquisite temperature control for optimal growth conditions. Future spin-spray design optimization specifically for the threshold temperature of $\sim 90^{\circ}\text{C}$ will be accomplished by the implementation of high-performance programmable peristaltic pumps to minimize flow rate fluctuations. A new array of large cone angle nozzles will also be added to provide optimal uniformity in spray coverage of the substrate. Finally, a two-point temperature sensing control loop will be incorporated to monitor the substrate (via physical thermocouple contact) and the wetted surface (with an infrared pyrometer) to allow feedback and predictive control of thermal fluctuations. These finer details are required to produce our magnetic films with the smoothness, adhesion and uniformity necessary for deposition over existing microelectronics.

We recommend future studies on the quantitative relationship between atmospheric and solution oxygen concentrations and the ferrite's magnetic properties. This will lead to a greater understanding of the relative importance of each competing reaction mechanism. This will require better oxygen control and sensing, necessitating the construction of a more sophisticated reaction chamber. This again points to the success of our highly cost-effective process design that achieved the desired objectives.

References

- 1) Adam, J. D.; Krishnaswamy, S. V.; Talisa, S. H.; Yoo, K. C. "Thin-Film Ferrites for Microwave and Millimeter-wave Applications." *J. Magnet. Magn. Mater.* **1990**, 83, 419-24.
- 2) Yoo, K. C.; Talisa, S. H. "Spin-Spray Plating of Spinel Ferrite Films on Semiconductor Substrates." *Electro-optical Materials for Switches, Coatings, Sensor Optics and Detectors* **1990**, 1307, 134-42.
- 3) Abe, M.; Tamura, Y.; Oishi, M.; Saitoh, T.; Itoh, T.; Gomi, M. "Plating of Ferrite Film on 8" Disc at 70°C by "Spray-Spin-Coating" Method." *IEEE Trans. Magn.* **1987**, MAG-23, 3432-35.
- 4) Matsushita, N.; Chong, C.P.; Mizutani, T.; Abe, M. "Ni-Zn Ferrite Films with High Permeability ($\mu'=\sim 30$, $\mu''=\sim 30$) at 1 GHz Prepared at 90°C ." *J. Appl. Phys.* **2002**, 91, 7376-78.

IV. Accomplishments

1. Publications: Nemec, A.T.; Gee, S.H.; Hong, Y.-K.; Aston, D.E. "Investigation of Temperature Effects on Spin-Spray Plating of Nickel and Iron Ferrites." *Ind. Eng. Chem. Res.* In preparation.
2. Presentations (contributed): "Low-Temperature Spin Spray Chemical Growth of Magnetic Ferrite Films." *ACS 78th Colloid and Surface Science Symposium*, Yale University, New Haven, Connecticut, June 20-23, 2004.
3. Number of graduate students supported: 1
Number of undergraduate students supported: 3

Fabrication of Inductors: Lithography and Materials Deposition

Christopher A. Berven
Department of Physics

I. Abstract

Fabrication of the test structures will be carried out on site using the methods of electron beam lithography and optical lithographic processing. Electron beam lithography is extremely well suited to the development of test structures where the geometry of a device must be optimized. Metal deposition techniques available on in the shared clean-room facility and elsewhere on campus include thermal and electron beam evaporation (to be purchased) and a sputtering system. For subtractive processing, an electron cyclotron resonance etching system is available in the clean-room facility. The clean-room facility also has a new mask aligner for performing optical lithography.

II. Approach and Results

The University of Idaho currently, has the capability to do electron-beam lithography (EBL)¹ and will soon have the capability to perform optical lithography. Using optical lithography features as small as 5 μm can be reproduced. EBL can create patterns and features with sizes as small as 50 nm, about 100 times smaller than optical techniques. Once the pattern has been reproduced in the resist material coating the substrate, the final structure will be created using additive (metal coating) or subtractive (etching) processes.

Both of these tools and procedures will be enclosed in a jointly operated cleanroom facility on the University of Idaho campus. Prof. Chris Berven is the manager of the electron beam lithography system and is a primary consultant for the organization and running of the cleanroom. Prof. Berven has been performing electron beam lithography for over ten years and has extensive cleanroom experience performing both additive and subtractive processes to devices created using optical lithography.

Electron beam lithography is an especially appropriate tool for making the test structures that will be used here. As the project progresses, modifications to the experiment can easily be incorporated into the test structures and fabricated. This process can be as short as one or two days. The most important advantages of EBL are the range of feature sizes that can be made (as small as 30 nm up to 100's of microns) and the ease of making structures with complex geometries. The basic steps in the EBL process are illustrated in Figure CB1. After spin coating and baking, the resist (PMMA) it is exposed using an electron beam. The exposed resist is then removed by immersion of the complete wafer in the developing solution. This results in a reproduction of pattern. At this point the details of the fabrication will differ.

For simple lift-off the whole wafer is now coated with metal so that only where the resist was removed is the metal in contact with the substrate. To finish the lift-off process the remaining unexposed resist and the metal over it are removed by immersion

in acetone leaving a reproduction in metal of the originally exposed pattern. This is shown in figure CB1 (c) and CB1 (d).

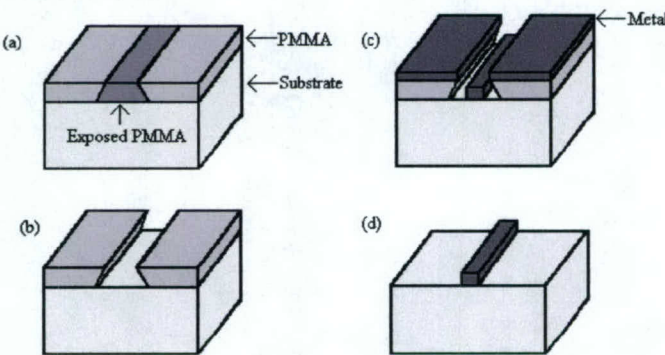


Figure CB1:

The basic steps of electron beam lithography. (a) Exposure of the resist. (b) Removal of exposed resist by immersion in the developer. (c) Wafer coating with metal. (d) Lift-off of remaining unexposed resist and the metal leaving a metal reproduction of desired pattern.

The technique of lift-off is very simple and takes a minimum of effort to create arbitrary metal patterns on the substrate. An example of the complexity and ease of complex pattern creation is shown in Figure CB2. Figure CB2 shows a demonstration lithography that used the lift-off technique combined with EBL to create a logarithmic spiral antenna test structure. It was created by Prof. Berven while he was working as a postdoctoral research associate at Dartmouth College using an EBL system similar to the University of Idaho system and also controlled using NPGS. This particular lithography was created on the first attempt. The metal deposited was 5 nm of Cr followed by 45 nm of Au. The minimum line width is approximately 200 nm, although line widths as small as 30 nm are routinely possible. The spirals have shapes that are true logarithmic spirals, not approximations using trapezoids or other simpler curves. This lithography demonstrates the ease fabrication (on the first attempt) and the arbitrary shapes (true logarithmic spirals) that can be made using the EBL system at the University of Idaho. The only major difference in the EBL systems at the University of Idaho at Dartmouth College is the University of Idaho system has a new digitally controlled scanning electron microscope (SEM) and the Dartmouth system has an older analog SEM.

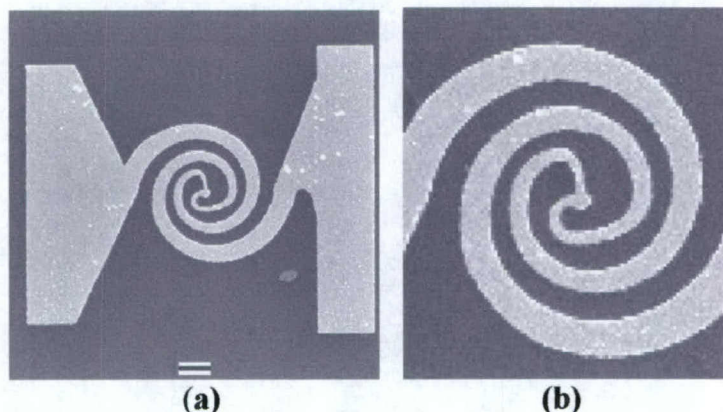


Figure CB2

(a) A logarithmic antenna test structure fabricated using EBL and lift-off. The scale marker at the bottom is 1 micron. The metallization layer consists of 45 nm Au on 5 nm Cr on top of a SiO₂ substrate. The minimum line width is about 200 nm. (b) Close up of the spiral structure. The pixelation is an artifact of the digital image acquisition. On this scale the edges are smooth.

The lift-off technique is very useful but can be limited to use with only certain materials. To use it, metal must be deposited from a point source far away from the substrate (relative to the thickness of the resist) so that the metal casts a shadow on the substrate. The method of deposition for the 'shadow' technique is via evaporation. Metal evaporation can be accomplished using thermal heating or heating with an electron beam. The University of Idaho cleanroom will have both thermal and electron beam evaporation systems installed. For some materials such as high melting point, compound materials or oxides, evaporation will not work. In these cases coating by sputtering must be used. Because of differences in the physical coating mechanism, alternate processing in the lithography must be used.

The sputtering process is performed at pressures at about 1 Torr which results in a short mean-free path of the sputtered material. Because of the short mean-free path, the apparent source of the material is non-localized. This gives good step coverage, i.e. resist side-wall coverage. Because of the step-coverage, lift-off is extremely difficult with sputtered layers. When sputtering is required, a modified lithography procedure must be used. Unlike with the lift-off processing, a substrate is first coated with the sputtered material and then covered with resist. A negative image of the desired pattern is reproduced in the resist with the EBL system. At this stage, the open areas are exposed and the substrate is inserted into a reactive ion etcher to etch away the exposed (unwanted) material, leaving the desired pattern under the protective layer of the resist. This process is shown in Figure CB3.

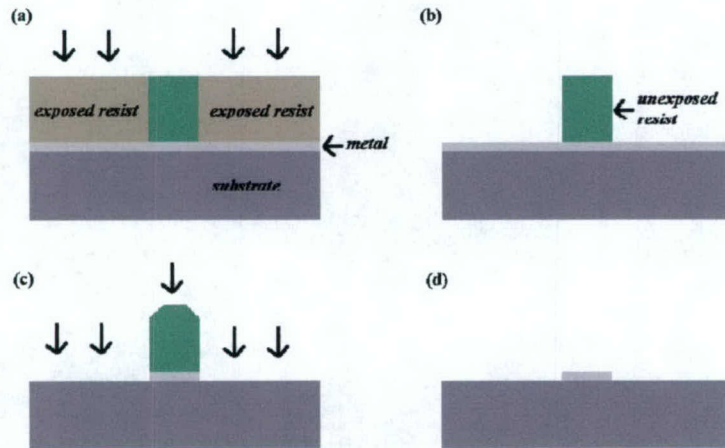


Figure CB3

Illustration of the EBL/etching process to be used with metals deposited using sputtering. (a) After the metal has been deposited, the resist to be removed is exposed. (b) The exposed resist is removed. (c) Etching is used to remove the undesired metal. (d) The final layer of protective resist is dissolved leaving the final pattern in metal.

To make inductors in a planar geometry, the issue of connectivity must be addressed. After the wire spirals inward it must be brought back out to so that connection can be made to the rest of the circuit. We propose two solutions to this issue, a buried exit lead and an air-bridge. Both of these solutions can be implemented using the facilities at the University of Idaho. The final choice of geometry for the leads will be chosen in conjunction with the members of this collaboration who are responsible for circuit design.

The buried exit lead would use a radial lead buried into a trench etched into the substrate and then covered by an insulator to electrically insulate it from the rest of the inductor. This process would require multiple steps consisting of etching, metal deposition, passivation, removal of excess insulator material and opening of vias to the ends of the underlying lead. After these steps are performed, the rest of the inductor is fabricated on top. This processing strategy is illustrated in Figure CB4.

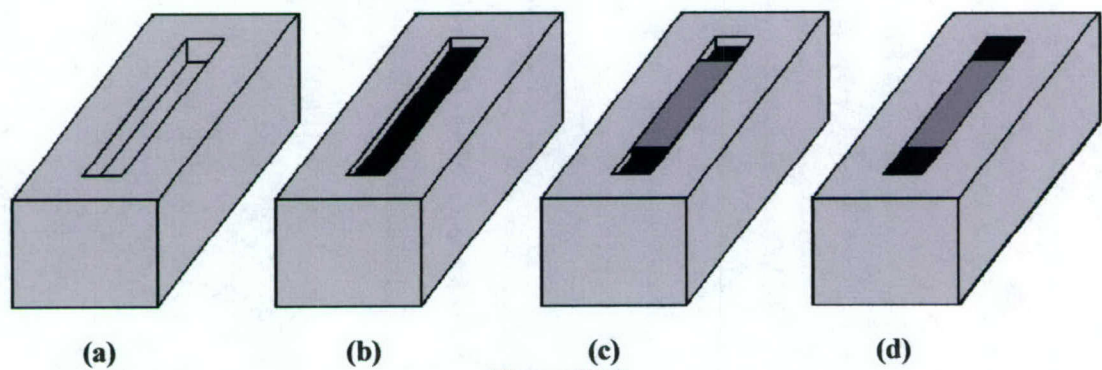


Figure CB4

The steps for making a recessed interconnect. (a) The etched trench. (b) The trench partially filled with metal. (c) The recessed interconnect partially covered with insulator. (d) The recesses at the ends of the recessed interconnect filled with metal bringing, it to the surface.

The other method by which to overcome the connectivity issue is to use air-bridge technology. This has been incorporated into EBL processing for many years. This technique has connects the inside termination of the inductor by a metal bridge suspended over the inductor. The advantage of this process is that it only requires one EBL processing step. This is done by using two layers of resist; the bottom one much less sensitive to exposure by the electron beam than the one on top. A dose from the electron beam that is greater than the critical exposure for the top layer but smaller than the critical exposure of the bottom resist will recreate a pattern only in the top later. A larger dose, greater than the critical exposure for both resists, will create a pattern in the resists that when developed will expose the substrate. A demonstration of this process is shown in Figure CB5. Here a contact with a radius much smaller than 1 μm has been located between two laterally opposed leads using this technique².

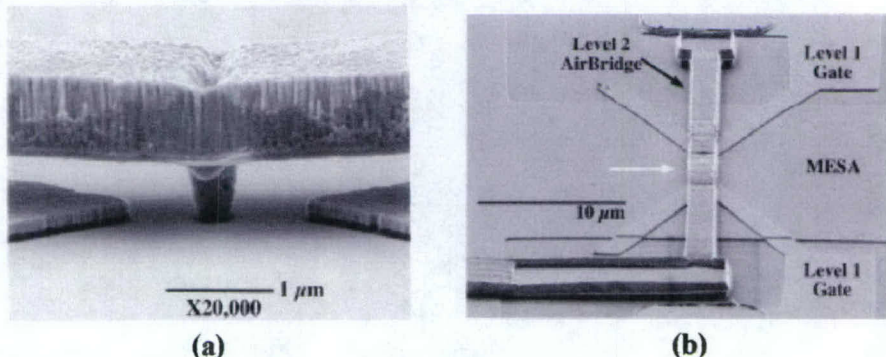


Figure CB5

SEM micrographs of airbridge fabricated using EBL. (a) Side view of the airbridge. (b) Overhead view of airbridge. The white arrow shows the direction from which the micrograph in (a) was taken. (from Sherwin et al.)

Both the air-bridge and buried lead techniques require registration of subsequent processing steps and patterns to the previous layer. This is accomplished using the alignment capabilities of the NPGS lithography system. With it, depending on the magnification chosen at which to do the alignment, accuracies of 30 nm, equal to the minimum line width achievable with an electron beam using standard lift-off techniques, are possible.

Electron beam lithography can be an extremely powerful tool for the fabrication of electron test structures. The ability to reproduce complex patterns with little time or materials overhead costs is ideal for research into novel planar inductors. The ease of incorporating new design ideas into existing structures means that many avenues can be explored during the duration of the project. Also, theorists designing the test structures will be able to get extremely rapid feedback on their ideas because of the minimal time delay between design of a new structure and the final fabrication of it. With the EBL and with the many fabrication tools in the University of Idaho cleanroom, there are very few limitations on what can be made giving full freedom to the designers.

The graduate student assigned to the project was trained to use the electron microscope in order to perform the electron-beam lithography necessary to make the test patterns of the inductors. This was necessary since the undergraduate who had been the principal operator of the electron microscope left in Spring of 2004 and teaching someone to perform electron-beam lithography is a very involved process. We were able to recreate some of the desired patterns of planar inductors of concentric ring pattern,

Fig. 1. We were also been able to do preliminary work on the fabrication of 'air-bridges' that will make the connection from the inside of the spiral pattern to the outside. This is a new technique for this group that has opened up many new possibilities of new geometries with which to make inductors. The first attempt at making an air-bridge is shown in Fig. 2. The picture is of an array of air-bridges fabricated using a range of design parameters in order to select the optimal combination for final assembly of the inductors. The development of the air-bridge technology was expected to expand the research into making lateral inductors instead of planar inductors. Figure 3 shows a schematic of a lateral air-bridge inductor. A lateral inductor has very different geometry than the planar design and could have much more utility in functional devices because of the higher efficiency of the lateral spiral geometry and its relatively compact footprint as compared to the lateral spiral pattern.

We were also able to construct an automated CAD program for the drawing of the circular spiral patterns.

Much of the electron beam lithography work was halted during the summer of 2004 due to problems with the maintenance of the electron microscope used for the electron beam lithography. Once the electron microscope was operational, fabrication of the spiral structures was taken over by Dr. Hong and his assistant.

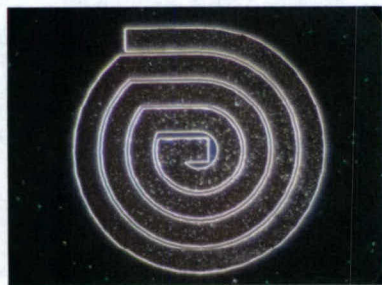


Fig. 1

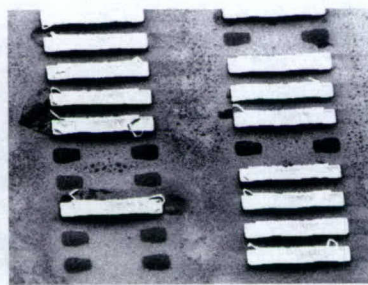


Fig. 2

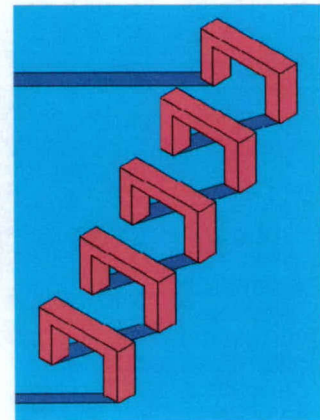


Fig. 3

III. Conclusions

The feasibility of constructing planar inductor patterns using electron beam lithography was shown to be possible through the construction of preliminary test structures. In addition, the ability to fabricate metallic airbridges was shown to be possible. The airbridges were determined to be highly useful as solutions for the problem of connecting the end of the inductor trace on the outside of the spiral to the other end of the inductor trace on the inside of the spiral. In addition, the development of the airbridge gave rise to the idea of creating a lateral spiral inductor (as shown in Fig. 3) that could have the advantages of a smaller footprint in the a circuit and a more compact and possibly more efficient design.

References

- ¹ Nanometer Pattern Generation System (NPGS). See www.jcnabity.com for more information.
- ² M. E. Sherwin, J. A. Simmons, T. E. Eiles, N. E. Harff, and J. F. Klem, 'Parallel Quantum Point Contacts Fabricated with Independently Biased Gates and a Submicrometer Airbridge Post', *Appl. Phys. Lett.*, **65** 2326 (1994)

IV. Accomplishments

Important preliminary design and fabrication were finished. Unfortunately, because of the maintenance problems with the electron microscope, these initial accomplishments could not be capitalized as soon as desired. The development of the skills to create the airbridge structures gave the design team a valuable new approach of solving the connectivity issue. This tool was discussed many times between Dr. Berven and Dr. Hong's assistant during meeting to plan future approaches to the fabrication of the inductors.

1. Publications

None

2. Patents:

None

3. Presentations (invited - contributed):

None

4. Honors

None

5. Number of graduate students supported: 2

Number of Post-doctoral students involved: 0

Number of undergraduate students supported: 1

Number of under-represented members by group: 1

Design, Analysis and Characterization of High-Q, High-L, Microwave, Magnetic Thin-Film Inductors

Jeffrey L. Young and Jon Watkins
Department of Electrical and Computer Engineering

I. Abstract

Discussed herein are the results associated with an extensive set of simulations of various planar and non-planar microwave inductors. Various inductor topologies were considered over the course of the project; some of the more successful topologies are reviewed below. Based upon these simulations, we believe that high-Q, high-L inductors can be realized using both magnetic and non-magnetic films. As anticipated at the outset of this program, there are trade-offs between L, Q and the frequency response. Particularly, for a given substrate thickness and magnetic film, the frequency response decreases as the inductance increases; Q decreases as the number of turns increases.

II. Project Objectives:

A principle objective of this project is to devise a microwave inductor using thin-film, magnetic material technology. It is desired that the device remain inductive, with very little capacitive or resonant effects occurring over the frequency range of DC to 3.0 GHz. It is also desired that the inductance of the device exceed a value of 50 nH and the quality factor (*Q*) exceed a value of 50; both of these values are considerably higher than those values reported in the open literature for the frequency range DC to 3.0 GHz. To accomplish this specific objective, the following sub-objectives were identified in the research proposal:

- Devise suitable inductor topologies;
- Devise equivalent circuit models that predict the linear performance of the inductor;
- Develop finite element and finite difference software simulations that predict the full electromagnetic response of the device;
- Investigate the non-linear performance of the magnetic thin-films and determine the required current to saturate the films;
- Develop a procedure for thin-film inductor design;
- Fabricate a thin-film inductor;
- Measure the inductance, frequency response and the quality factor of the fabricated thin-film inductor; measure the saturation current;
- Publish research results and outcomes in peer-reviewed journals (such as the *IEEE Transactions on Microwave Theory and Techniques*).

As can been seen in the discussion below, all but a few of these objectives have been realized. The fabrication of an inductor, also part of this effort, is reported in separate sections authored by Prof. Hong and Prof. Berven.

III. Approach

The primary approach adopted in this investigation is one of numerical simulation of the electromagnetic field associated with a given inductor topology. Three numerical tools were considered for the quantization of Maxwell's equations: 1) Ansoft's High Frequency Structure Simulator (HFSS), 2) Sonnet Circuit Simulator and 3) a Finite-Difference, Time-Domain (FDTD) simulation tool, which was developed at the University of Idaho. Given its flexibility and accuracy, HFSS was the primary tool used in the investigations.

Various inductor topologies were considered such as the spiral, toroid, and stacked-toroid inductors. In addition to these topologies, ferromagnetic films were strategically incorporated into the design in such a way as to potentially improve the quality factor Q and/or the inductance L . Energy loss mechanisms within the dielectric and the magnetic material were included in many of the simulations. Typically, a planar inductor rested on a $740 \times 740 \times 300$ micron silicon substrate; a gold trace of width 20 microns and of thickness 2 microns was used to conduct an electrical current. For the spiral inductors, the gap spacing between traces was typically 3 microns, and the inner and outer diameters were 60 and 172 microns, respectively. Each inductor had a ground ring surrounding it. The ground ring was incorporated for testing purposes and was placed far enough away from the traces to render its effect negligible.

The numerical solvers were programmed to compute the scattering parameters of the inductors; a post-processing numerical algorithm developed at the University of Idaho was then used to extract L and Q as a function of frequency, as determined from a Pi or Tee circuit model. Table 1 shows a tabulation of the results for twenty different cases; here $L(\text{dc})$ is the inductance at DC and $Q(\text{max})$ is the maximum Q at resonance; the resonant frequency is also provided. Each case is briefly described below.

Case	$L(\text{dc})$	$Q(\text{max})$	Resonance
1	5.28 nH	8.84	5.4 GHz
2	5.5 nH	8.8	5.4 GHz
3	4 nH	11.56	6.6 GHz
4	5.6 nH	8.91	4.8 GHz
5	8.38 nH	11.39	3.89 GHz
6	16.9 nH	32	2.3 GHz
7	10.3 nH	11.46	3.61 GHz
8	7.8 nH	42.8	4.4 GHz
9	5.94 nH	20.3	5.57 GHz
10	5.75 nH	12.23	5.4 GHz
11	n/a	n/a	n/a
12	6.1 nH	13.5	11.32 GHz
13	5.17 nH	13.3	12.75 GHz
14	29.6 nH	12.75	5.2 GHz
15	1.77 nH	16.8	18.3 GHz
16	1.56 nH	16.46	19.72 GHz
17	32 nH	17.1	4.56 GHz

18	5.84 nH	1.6	5.63 GHz
19	5.63 nH	1.55	5.38 GHz
20	5.71 nH	1.52	5.19 GHz

Table 1. Case study results

Cases 1 and 2: These cases are associated with the spiral inductors of Figures 1 and 2, and are used to establish a benchmark for typical values. Both inductors are regarded as concentric ring inductors with 4.75 turns. No magnetic material was used in these inductors. The cases differ only by the placement of the bond pads in order to ascertain their effect on L and Q. Per Table 1, no significant effect was observed by moving the pads about the substrate. For both cases the DC inductance is about 5.4 nH and the maximum Q is 8.8; the inductor tends to resonate at about 5.5 GHz, which suggests that its usable bandwidth for a flat inductive response is about DC to 3.0 GHz.

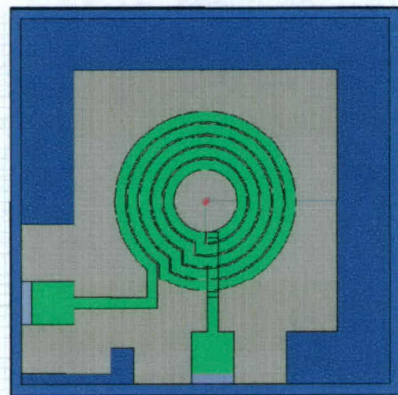


Figure 1: A 4.75 turn, concentric ring spiral inductor.

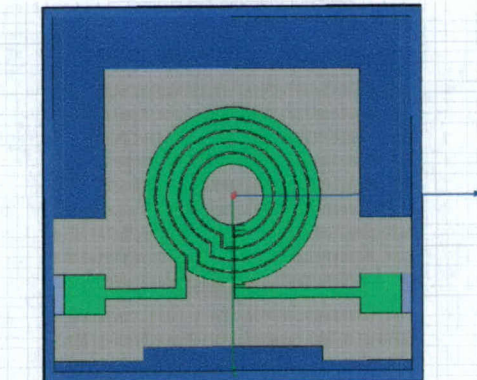


Figure 2: A 4.75 turn, concentric ring spiral inductor.

Case 3: This inductor is a 3.75 turn spiral with the bond pads on opposite sides of the substrate, as shown in Figure 3. Since there are fewer turns to this inductor relative to the inductors of Cases 1 and 2, the inductance value decreased to 4.0 nH while the Q and

resonant frequency increased to 11.56 and 6.6 GHz, respectfully. These observed decreases and increases are consistent with theory.

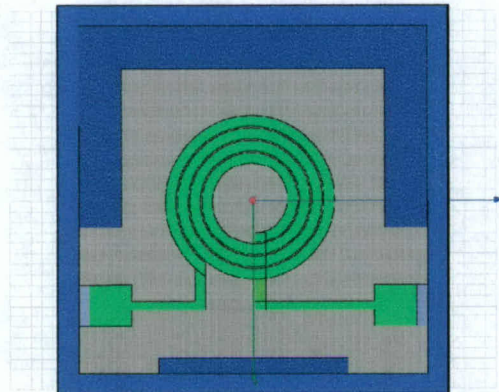


Figure 3: A 3.75 turn, pure spiral inductor.

Cases 4, 5, 6 and 7: Each inductor associated with these cases is a 4.5 turn square spiral with bond pads on opposite sides of the substrate as shown in Figure 4.

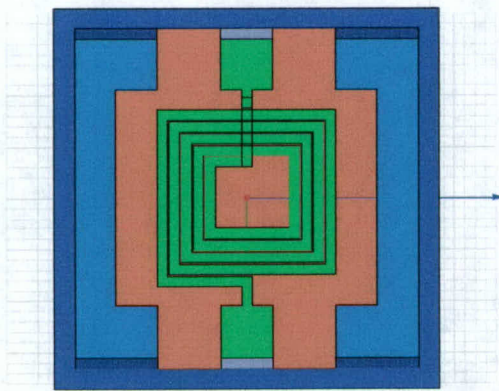


Figure 4: A 4.5 turn, square spiral inductor.

Case 4 establishes a benchmark for a square spiral inductor without any magnetic material. In Case 5 a 1 micron ferromagnetic film is placed between the dielectric substrate and the copper traces. The magnetic material has an assumed relative permittivity and permeability of 12 and 100, respectively. Case 6 has a 1 micron ferromagnetic substrate and superstrate; Case 7 has a 5 micron ferromagnetic substrate. The ferromagnetic slabs are assumed to be lossless. As expected, with the addition of the ferromagnetic film slab, the inductance and Q both increase significantly. However, due to the increased inductance, for an otherwise fixed capacitance for all of these cases, the resonant frequency also drops significantly by a factor of two. The only way to decrease the capacitance, and hence increase the resonant frequency, is to increase the silicon thickness. Whether or not this is possible depends on the microelectronic process.

Cases 8, 9, 10 and 11: These square spiral inductors consist of 2.5 turns of copper; a depiction of one such inductor is shown in Figure 5.

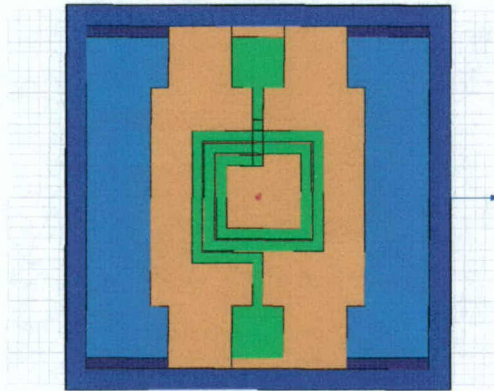


Figure 5: A 2.5 turn, square spiral inductor.

For Case 8 a 1 micron, lossless ferromagnetic superstrate and substrate film was used. Case 9 has the same superstrate and substrate films as Case 8 except for the inclusion of an additional 2 micron silicon dioxide layer. Cases 10 and 11 consider the effect of magnetic loss and have the same configuration as that of Case 9. The loss in ferromagnetic film is assumed to be constant over all frequencies in Case 10. The relative permeability of the film is 100 with a magnetic loss tangent of 0.05; the relative permittivity is 12 with a dielectric loss tangent of 0.01. In Case 11, the ferromagnetic permeability is a function of frequency. The dielectric loss tangent is the same as before, but the permeability is defined by the following second-order equation:

$$\mu_r = \mu_\infty + \frac{(\mu_s - \mu_\infty)\omega^2}{\omega_0^2 + 2j\alpha\omega\omega_0 - \omega^2}$$

where,

$$\mu_s = 100$$

$$\mu_\infty = 1$$

$$\alpha = .076$$

and

$$\omega_0 = 2\pi(6 \times 10^9)$$

Case 11 did not reach numerical convergence due to the excessive amount of detail in the geometry and in the material model. For this reason, "n/a" is entered in Table 1. It is observed from Table 1 that high Q high resonance can be achieved with strategically placed ferromagnetic films using traditional spiral topologies. The films do not, however, seem to have a strong impact on the inductance. It is surmised that the magnetic film does not create a path by which all the magnetic flux is linked to the copper traces. For this reason more exotic topologies were considered, as described next.

Case 12: This case considers a 6 turn, square toroid inductor with a solid ferromagnetic film core, as shown in Figure 6.

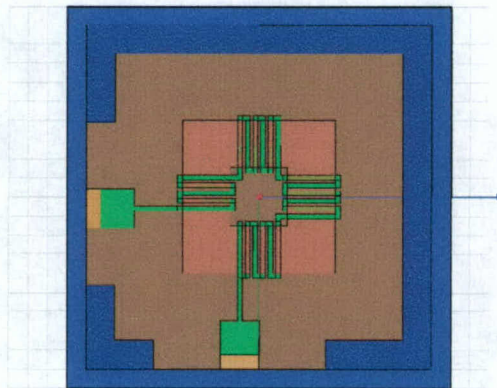


Figure 6: A 6 turn, square toroid.

The inductor is composed of parallel copper traces that wrap the ferromagnetic core. These traces run perpendicular to the ferromagnetic film to create an optimal coupling of the magnetic flux to the film. The toroid is separated from the ground plane by a silicon substrate that is 740 x 740 x 100 microns. The toroid is square with an inner dimension of 50 microns and an outer dimension of 170 microns. The ferromagnetic film is assumed to be lossy with a relative permeability of 100, a magnetic loss tangent of 0.05, a relative permittivity of 12, and a dielectric loss tangent of 0.01. The silicon and ferromagnetic films are assumed to have a bulk conductivity of 0.01 S/m, and the copper has a bulk conductivity of 58000000 S/m. Although this topology did not significantly alter Q and L, it did in fact increase the resonant frequency to 11.3 GHz. The primary cause of this increase is the significant decrease in the capacitance, due to the relatively small effective area of the copper traces. This conclusion suggests that extremely wideband, low-L inductors are feasible to manufacture when ferromagnetic film cores are used.

Case 13: This case is the same as Case 12 except that the core is composed of ferromagnetic rings, shown in Figure 7. These rings were incorporated to see if eddy currents losses were significant. From the data in Table 1, it appears that ringed core has an insignificant effect on loss.

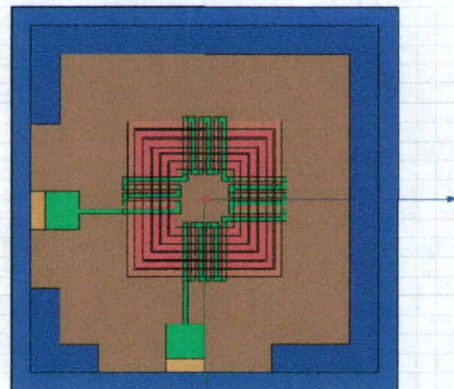


Figure 7: A 6 turn, square toroid with a ringed core.

Case 14: A 22 turn square toroid inductor with a solid ferromagnetic core is considered in this case, as shown in Figure 8. The copper traces are angled to fit more turns of copper about the core. As expected, a significant increase in the inductance is obtained without compromising the Q. The resonance frequency is above 5.0 GHz, which is also satisfactory.

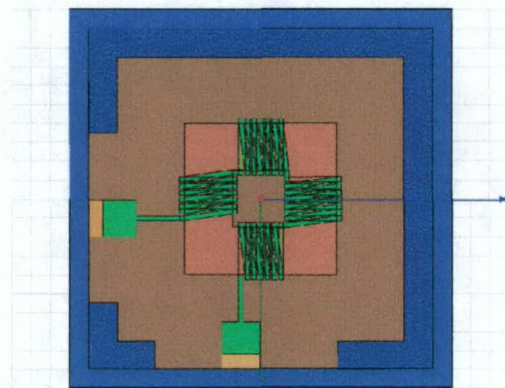


Figure 8: A 22 turn, square toroid.

Case 15: Next consider a 6 turn, circular toroid inductor with a solid ferromagnetic film core. The inductor is composed of wedge shaped copper traces on both the top and bottom, as shown in Figure 9.

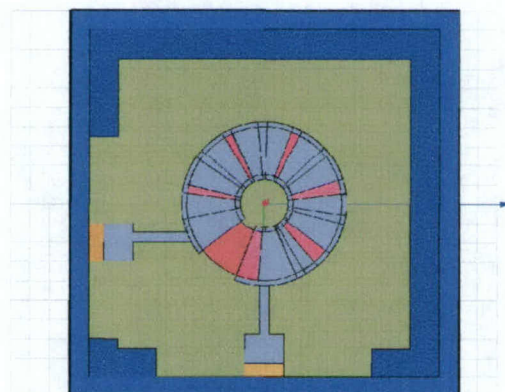


Figure 9: A 6 turn, circular toroid.

The circular toroid is separated from the ground plane by a 740 x 740 x 100 micron silicon substrate. The toroid is a circle with the inner radius of 25 microns and an outer radius of 85 microns. The ferromagnetic film is assumed to be lossy with a relative permeability of 100, a magnetic loss tangent of 0.05, a relative permittivity of 12, and a dielectric loss tangent of 0.01. The silicon and ferromagnetic film are assumed to have a bulk conductivity of 0.01 S/m; the copper is assumed to have a bulk conductivity of 58000000 S/m. As Table 1 suggests this inductor has a superior resonance characteristic (i.e., resonant frequency of 19.72 GHz) and high Q but very low inductance. The inductance could be potentially increased at the expense of Q with more wedge-shaped sections.

Case 16: This case is the same as Case 15 except with a ringed ferromagnetic core, as shown in Figure 10. As before, the ringed core does not seem to have an appreciable effect on performance.

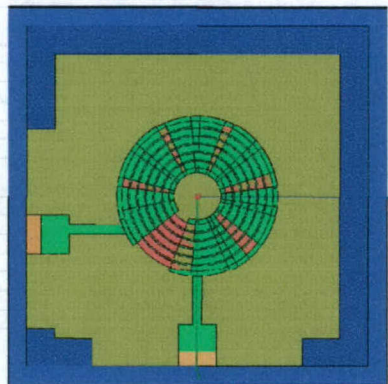


Figure 10: A 6 turn, circular toroid with ringed core.

Case 17: An 11 turn, 3D toroid inductor with a solid, ferromagnetic film core is considered for this case, as shown in Figure 11. The inductor is composed of rectangular copper traces that wrap around the ferromagnetic core. Separating the toroid from the ground plane is a 740 x 740 x 100 micron silicon substrate. The toroid is rectangular with an inner dimension of 38 microns and an outer dimension of 82 microns; it rises 140 microns off the substrate. The ferromagnetic film is assumed to be lossy with a relative permeability of 100, a magnetic loss tangent of 0.05, a relative permittivity of 12, and a dielectric loss tangent of 0.01. Due to the vertical orientation and the large core cross-sectional area, the inductance of this device is 32 nH. It is doubtful, however, that this device could be fabricated using current silicon processes.

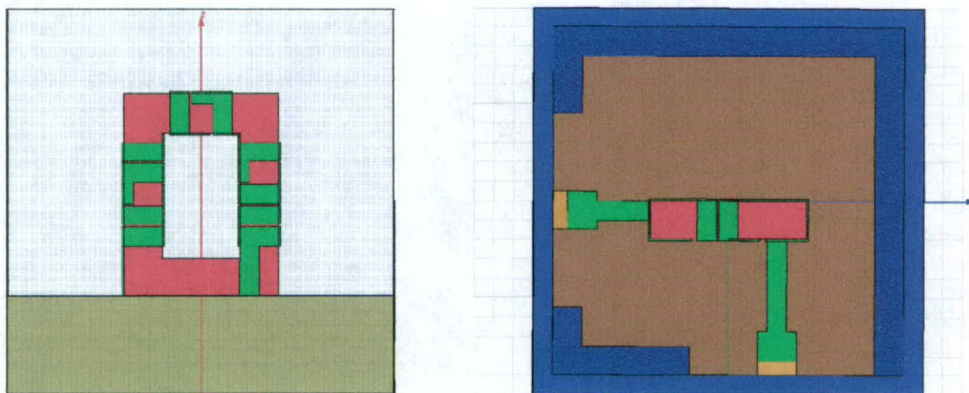


Figure 11: A 3D toroid: side view (left) and top view (right).

Cases 18, 19 and 20: The next topologies are designed to have the same dimensions as the actual hardware that has been proposed to be tested. Cases 18, 19, and 20 are 4 turn, concentric ring spirals. Case 18 has via holes connecting the top ground plane to the

bottom ground plane. Case 19 has indium strips (conductivity of 6440000 S/m) acting as external vias connecting the top and bottom ground planes. Case 20 has no via holes connecting the top and bottom grounds. Case 20 was simulated for comparison purposes to see if the addition of the via holes made a difference in the results given from HFSS. Figure 12 shows the topology of Case 18.

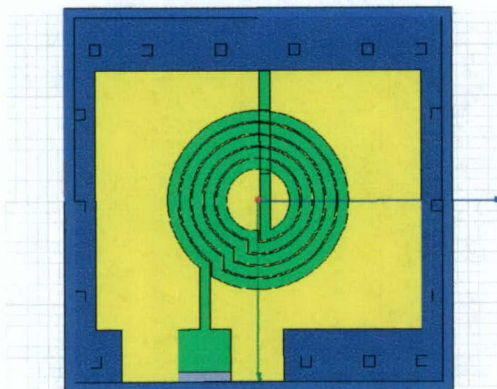


Figure 12: A 5 turn, concentric ring inductor.

A top ground ring surrounds the entire inductor. Port 2 is connected directly to the ground ring to create a short circuit. The inductor rests on a 740 x 740 x 299 micron silicon substrate separated by a 1 micron oxide layer. The gold trace has a width of 20 microns and a thickness of 100 nm. The gap spacing is 3 microns with an inner diameter of 60 microns and an outer diameter of 172 microns. A 10 nm trace of titanium is placed on the substrate to help with the adhesion of the gold. Since the trace thickness is much smaller than in the other cases, the Q is smaller due to the increase in the resistance. This conclusion is confirmed by the results in Table 1.

IV. Conclusions:

Numerous topologies have been investigated, with many of them showing promise for being realized in hardware in the future. Inductance values ranging from 5 nH to 40 nH seem possible with corresponding Q values ranging from 5 to 20. A flat frequency response up to about 3.0 GHz is equally possible. It was desired at the beginning of the project to test some of these designs using processes developed by other team members. Unfortunately this did not occur, due to process problems experienced by the other team members. Even so, the simulation data is regarded to be an accurate quantization of the inductors and any experimental data gathered in the future is expected to show little deviation.

The principle issues associated with the design of high-Q, high-L, wideband inductors are the minimization of stray capacitance and the minimization of copper, film and dielectric losses. The capacitance can be reduced by using thicker substrates. The thickness, however, is not set by the inductor designer but by the fabrication process. Hence, further minimization of the stray capacitance is unlikely. Copper loss is reduced by using thicker

and shorter conductors. Again, thickness is controlled by the fabrication process. Shorter conductors can be used by employing high quality ferromagnetic films with high permeabilities. This is indeed possible, but additional work of constructing low-loss, high- μ films is still needed.

Various circuit models were constructed to show the impact of capacitance, mutual inductance and self inductance on the overall performance of the inductor. These models, along with the model parameters were transferred to the team led by Prof. Greg Donohoe. (Further information regarding these models can be found in the report by his team.) His team demonstrated how such inductors could be tested on a VLSI chip by measuring the oscillation frequency of an on-chip oscillator.

During the course of this project the microwave laboratory was upgraded in anticipation of testing phase. A 26.5 GHz spectrum analyzer was acquired to perform linearity measurements and a ground-signal-ground probe was purchased to perform measurements using a Cascade probing station.

Not presented in this report is the development of new numerical simulation algorithm for the excitation and detection of electromagnetic signals. Further information regarding this effort can be found in the book chapter by Young and Adams; see Section V.A.b.

V. Accomplishments:

A. Refereed Publications:

- a) Refereed Journals: None
- b) Refereed Book Chapters: J.L. Young and R. Adams, "Excitation and detection of waves in the FDTD analysis of N-Port networks," *Progress in Electromagnetic Research*, vol. 53, pp. 249-269, 2005

B. Patents: None

C. Presentations (invited - contributed): None associated with this project.

D. Honors:

1. Appointed to the position of IEEE Antennas and Propagation Chapters Coordinator.
2. Served on the Steering Committee and the Technical Program Committee of the 2004 IEEE Antennas and Propagation Society International Symposium and USNC/URSI Radio Science Meeting, Monterey, California.
3. Co-chaired the Finite-Difference, Time-Domain session at the 2004 IEEE Antennas and Propagation Society International Symposium and USNC/URSI Radio Science Meeting, Monterey, California.

E. Support:

1. Number of graduate students supported: Two graduate students 2 (Jon Watkins and Ryan Adams)
2. Number of Post-doctoral students involved: Zero
3. Number of undergraduate students supported: Zero
4. Number of under-represented members by group: Zero

Integration Concepts for Magnetic Thin Film Inductors

Victor H. Coredero-Calle and Gregory W. Donohoe
Department of Electrical and Computer Engineering

I. Abstract

This effort examined methods for integrating the thin film inductors onto a Complementary Metal Oxide Semiconductor (CMOS) integrated circuit, where they can become part of on-chip microwave circuits. The selected method is to deposit the inductors in or above the upper metallization layer, making contact with the CMOS circuits below through vias. In anticipation of fabricating test samples, most of this effort was devoted to extracting circuit models of the proposed thin film inductors, and simulating their behavior on a test circuit, a voltage controlled oscillator. Using the SPICE circuit simulation software, we were able to demonstrate the function of the inductors in this circuit, which oscillated around 2.5 GHz.

II. Approach and Results

This phase of the research studied methods for integrating soft thin film inductors onto an active integrated circuit. The integrated inductors will supply the passive inductor components for monolithic, integrated radio-frequency circuits, particularly wireless communication nodes, operating in the 1 to 10 GHz region. The challenge is to integrate the inductors into the same package as the radio die (chip); ideally, the inductors will be integrated onto the silicon die itself. This effort combines aspects of circuit design and modeling, process engineering, and packaging.

The figure below shows the elements of an integrated circuit package. The silicon die (chip) containing the integrated circuitry is glued onto a ceramic or plastic package body. Copper or gold leads conduct signals from the die to the printed circuit board, which holds the many chips and other components that complete a system. Bond wires connect aluminum contact points called bond pads on the die to the package leads. The bond wires are bonded to the bond pads ultrasonically, thermally, or thermosonically.

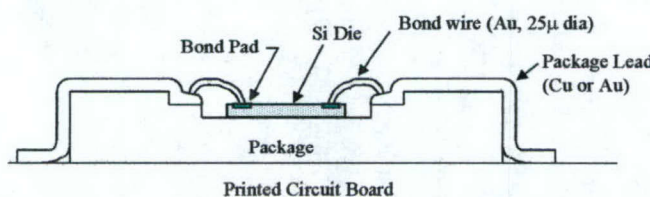


Figure 1: Integrated circuit package with die and interconnects.

The thin film inductors represent new components, which must be integrated into the chip-package system so that the inductors become part of the active circuitry on the chip. The integration must be manufacturable and durable, while maintaining acceptable manufacturing tolerances and not interfering with the function of the system. We have chosen to deposit the thin-film inductors above the final metal layer. Electrical contact is

made with the CMOS circuits below through the bond pads normally provided for bonding wires. The Figure 2 below shows a cross section of bond pad region of the chip with the inductor in place.

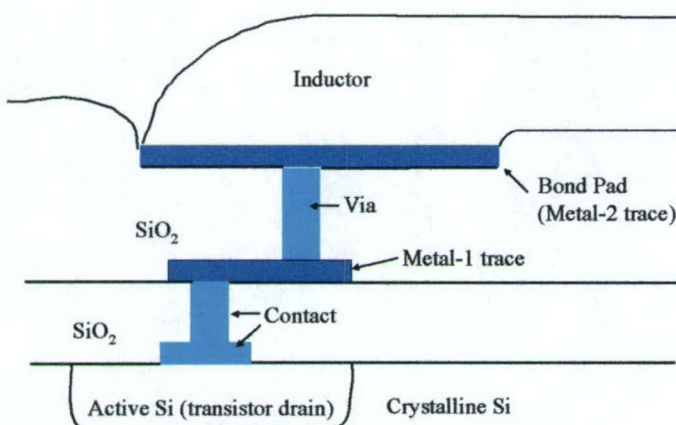


Figure 2: Integration scheme

The transistors are implanted into the crystalline silicon chip. Metal conductors are deposited above the chip, separated by oxide insulators. The entire chip is protected with a thick passivation layer, or overglass. Holes or vias are etched through the other oxide layers to admit conducting plugs, typically tungsten, which complete the electrical path to the active surface of the chip.

This “back end of process” approach has several

circuit fabrication from the thin

film deposition. The wafers will be fabricated up to the final metal layer in a commercial plant, then moved to our facility for the final metal layer, thin film inductors, and a passivation oxide. The wafers never re-enter the fabrication line, so there is no risk of contaminating the line with impurities introduced in the inductor step.

Test Circuits

The ultimate proof of the success of integration is to demonstrate the inductors working in an actual radio frequency circuit. The bulk of our effort was directed at creating a circuit model of the thin film inductors, designing a test circuit, and simulating the combination.

The Cross-coupled NMOS-LC Tank Oscillator circuit

For a test circuit we chose an oscillator topology gives good normalized phase noise compared. The quality of an LC tank oscillator relies on the LC block, and ideal oscillator has infinite Q at the LC tank. However our Q in the Square spiral-1u-

supersubstrate inductor is finite. A negative resistance will be needed to cancel the energy lost by the real part of the L-impedance (and of the rest of the components of the circuit).

In any RLC circuit the current consumption is inversely proportional to the inductance value, which implies that to get better phase noise we need to consume low power, with larger L with higher Q. Our Q values for

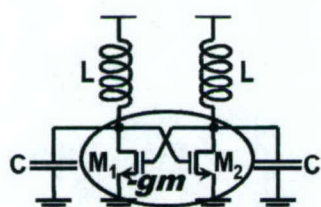


Figure 3: Negative resistance oscillator

the Honeywell-MOI5-inductor will depend on the operating frequency, as shown in table (1).

Figure 3 shows a negative resistance oscillator implemented with cross-coupled NMOS. Negative resistance is placed in conjunction with an LC Tank and will have the task of cancel the energy loss effects of our components for sustaining constant oscillation.

For analysis, the circuit can be simplified to the equivalent circuit of Figure 4, where C represents all the capacitance effects on the drain nodes of M1 and M2.

The negative resistance ($-1/g_m$ from M1 and M2) must replenish the energy losses by circuit resistances. Thus, the circuit can be schematized as an ideal LC oscillator like that in Figure 5.

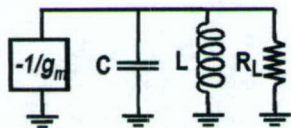


Figure 4: Equivalent circuit



Figure 5: Equivalent ideal tank circuit

This has an oscillation frequency of:

$$F = \frac{1}{2\pi\sqrt{L \cdot C}} \quad (\text{Eq 1})$$

In a more detailed view of the multiple capacitances (Figure 6) effects for the small signal circuit equivalent, we consider the following parameters: C_{gs} (gate source capacitance), C_{gd} (gate drain capacitance), C_d (drain capacitance) and the output impedance r_o . Figure 6 shows the representation of these parameters into a equivalent circuit schematic. Note that in the circuit C_{gd} is counted four times because a pair of them is used in a differential circuit structure).

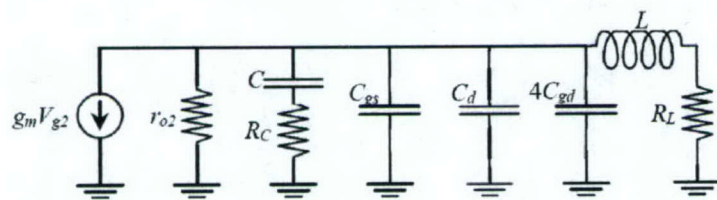


Figure 6: Equivalent circuit with parasitics

due to fabrication processes imperfections. The oscillation amplitude will not grow infinitely, since it will be limited by the clipping effects of the active transistors. When the amplitude grows over supply voltage, the positive resistance will grow and will pull down the amplitude to an equilibrium point. At this point a stable oscillation will be initiated and sustained. In order to sustain oscillation, we require that $1/g_m$ exceed the equivalent resistance of the load.

Now we require the negative resistance to be smaller than the overall parallel resistance of the tank circuit (which comprises the parasitic of the active and passive elements). We don't need to exactly match the negative resistance to the resistor losses, which can vary

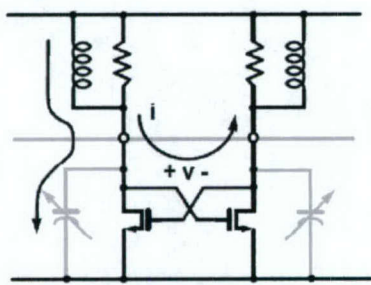


Figure 7: View of current dynamics in a cross-coupled circuit

During oscillation (Figure 7) when one of the output nodes (one of the transistors drains) is close to clipping voltage, one of the nodes is at high and the other at low. This causes one NMOS to turn off, and the other go to deep into the linear region. The higher into the linear region of that transistor, the lower absolute value of its gm (therefore its negative resistance falls), which will slow down and stop the amplitude growth on the output node. If the amplitude of the oscillations grows too much, the transistors will enter the linear

region. If they go too deeply into it, the resistance gate source will make the overall Q of the LC circuit decrease. It is on our best interest to keep the transistors in the saturation region, not making them any larger than that required to initiate and maintain oscillation.

Now we focus on the power consumption aspects, as shown in the equations 2, 3, 4 and 5. From here we can naturally arrive to the conclusion that the higher the inductor value (for an equivalent Q value), the lower drain current, consequently lower total power consumption.

$$\frac{1}{gm} = R$$

(Eq 2)

$$R = w_0 \cdot \frac{L}{Q}$$

(Eq 3)

$$gm = \frac{I_d}{v_{gs} - v_t}$$

(Eq 4)

$$I_d = Q \cdot \frac{V_{gs} - V_t}{w_0 \cdot L}$$

(Eq 5)

For this project we designed multiple oscillator circuits for different oscillating frequencies instead of having a variable capacitor (Figure 10). The reason is to fix steady one variable (capacitance) to be able to imply and deduce inductor behavior from the real resultant oscillation frequency obtained. The other possible approach would have been to implement a tunable oscillator (by doing a variable capacitor, approach used for integrated VCO designers), which would allow the oscillator to move around certain frequency range. But since it is the inductor characteristics (Figure 8) that we want to test, we will do only the first approach.

In our design, we use MOS capacitors (Figure 9), which are capacitors formed out of MOS transistors by coupling the drain to the source, and using the gate as a capacitor node and the shorted connection as the other node. To form a variable capacitor (within a narrow margin) what is done is to vary the drain source voltage. MOS capacitor typically are used on these designs since they reach very low capacitance values (required for high frequency oscillation frequencies according to equation 1)



Figure 8:
adjustable
parameters

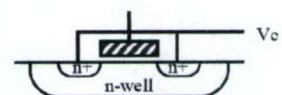


Figure 9: MOS capacitor

This design won't use capacitors plunged to ground for the high frequencies, since this would connect unwanted physical source capacitances, which consequently will make the LC tank – Q decay (and affect the final frequency).

Selected Thin-Film Inductor Design

Our test inductors were simulated thoroughly on the Ansoft Corp. High Frequency Structure Simulator (HFSS). This tool provides a complete design flow for electromagnetic devices. Of the many inductors developed in the project, we have chosen a square spiral with ferromagnetic film for our test circuit.

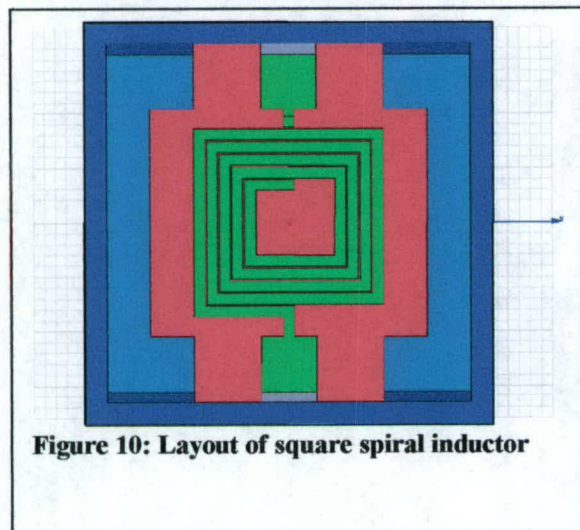


Figure 10: Layout of square spiral inductor

The 4.5 turn Square Spiral Inductor has bond pads on opposite sides of the substrate. The inductor sits on a 740 x 740 x 1 micron ferromagnetic film on the silicon substrate. There is also a 740 x 740 x 1 micron ferromagnetic superstrate. The inductor trace width is 20 microns. The gap spacing is 3 microns, and the metallization is gold. The inner diameter is 60 microns and the outer diameter is 172 microns. The relative permittivity and permeability of the ferromagnetic film is 12 and 100 respectively. The film is assumed to be lossless.

Using HFSS simulation data

The HFSS tool will give us the following parameters for each frequency point: R1short, R2Short, L1Short, L2Short, R1sh, R2sh, C1sh, C2sh, Q1, and Q2. These values will completely represent the inductor behavior despite they don't have a real world equivalent. Since we will need a physical model for simulation, a transformation is required. The proposed circuit model for the inductor is shown in Figure 11.

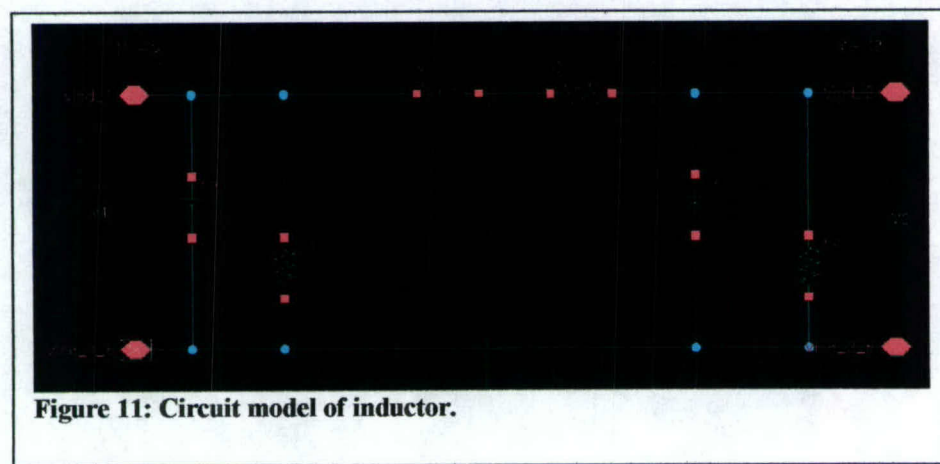


Figure 11: Circuit model of inductor.

Observe that this inductor will change to capacitive behavior at the frequencies in which any of its model-parameters change to a negative value. As we see, the inductance to capacitance turnaround occurs after we might be inferred by HFSS data and occurs between 3.5 and 3.75 gigahertz. (Table I)

Table I: physical parameter values for case (6) inductor.

F	1/Ga	1/Gb	Ca	Cb	Rs	Ls
GHz	ohms	Ohms	Nano farads	Nano farads	ohms	henries
0.5	8.595344198154E+04	1.240963336674E+05	1.280182579103E-04	8.842851488378E-05	2.837860564096E+00	1.866647164598E-08
0.75	8.236842615287E+04	1.172369421472E+05	1.284041248272E-04	8.834942242373E-05	3.058353249060E+00	1.900166370499E-08
1	7.714650892255E+04	1.099987048634E+05	1.289360744540E-04	8.825298846272E-05	3.382369992143E+00	1.951287653711E-08
1.25	7.110943891405E+04	1.019485984104E+05	1.296243704743E-04	8.813728181526E-05	3.792984611266E+00	2.023099465897E-08
1.5	6.496022190174E+04	9.317775987406E+04	1.305069119167E-04	8.797691923706E-05	4.358535888105E+00	2.120849763146E-08
1.75	5.845835866425E+04	8.486053852742E+04	1.315864413721E-04	8.778291833130E-05	5.132846206904E+00	2.253677212097E-08
1.9	5.473964734570E+04	7.989557590192E+04	1.323367331214E-04	8.764980510289E-05	5.732237823384E+00	2.355740828710E-08
2	5.218638919976E+04	7.666283904306E+04	1.328894356463E-04	8.754854879822E-05	6.222879599722E+00	2.435717303309E-08
2.1	4.967946097802E+04	7.380844185924E+04	1.334786360125E-04	8.744343185524E-05	6.776454378898E+00	2.527478226100E-08
2.3	4.495423549188E+04	6.793992012401E+04	1.347987756457E-04	8.720638834655E-05	8.250441316491E+00	2.756045212628E-08
2.5	4.032166664137E+04	6.280254755054E+04	1.363178770193E-04	8.692929095676E-05	1.045248184119E+01	3.070623921521E-08
2.75	3.500559384937E+04	5.689229043091E+04	1.385523484997E-04	8.652325866493E-05	1.533194746238E+01	3.671056814239E-08
3	3.004459660832E+04	5.170836183582E+04	1.412437704965E-04	8.604044107068E-05	2.649407240627E+01	4.749467330372E-08
3.25	2.549747503129E+04	4.726925734924E+04	1.445109206981E-04	8.546165478563E-05	6.423926634399E+01	7.207595676328E-08
3.5	2.128798900555E+04	4.338562340139E+04	1.485470536351E-04	8.476739933538E-05	4.424060345355E+02	1.803160442419E-07
3.75	1.743464312326E+04	4.032805344551E+04	1.536516671544E-04	8.393584667782E-05	8.169848694043E+02	-2.267292005446E-07

Oscillator models using the Thin-film Inductor

For simulation and layout the Cadence tool set was used. We defined an ideal composed block that will carry the modeled inductor for a particular frequency. The component library used to create the modeled inductor was cadence reference library. The inductor is modeled as a two port symmetrical network. A set of physical modeled inductors were created for this project. Once the schematic of a modeled inductor a particular frequency of interest is ready an instance is created, making the inductor a block. This block has three nodes since we had a common node on the 2 port network. The approach taken for obtaining the oscillator elements relied heavily on direct simulation. Once the inductor model was created for a particular oscillation frequency, the oscillator circuit was modified until the required oscillation frequency was reached.

Since we are using a cross-coupled NMOS LC oscillator, our design guidelines say that we should focus on getting enough negative resistance (-1/gm) to cancel the effects of the multiple resistances on the LC tank. Remember that the maximum amplitude will be taken care by the supply voltage and the crossed coupled array of NMOS. With this in mind, we now have the job of tuning the capacitor between the outputs (NMOS transistor drains).

Only for the 0.5 GHz oscillator, a pair of capacitors will be connected between the output and ground. This is because the required capacitance (at 0.5 GHz oscillation) has to be high. For the rest of the circuits a fully internal capacitor will be used between outputs, which will improve the endurance of the oscillator to external distortions (note that on the oscillator background section we used grounded capacitors). The common

node on the modeled inductor will be always sent to ground. Our simulator uses Spectre models for each of the instances included in the oscillator. The Spectre models, the layout and the schematic cell views come from the Honeywell MOI 5 process analog library.

The Spectre simulator will take into account all the parasitic capacitances and plug them into the equation of the oscillation response, this is why we say this design relies ultimately on simulation rather than hand based values.

For fine-tuning the oscillator frequency we modify multiple parameters such as the capacitance of the capacitor connected between the output and ground, or the number of NMOS put in parallel on the crossed coupled array (which will affect the total capacitance of the LC tank), or we change the width/length proportion of these same transistors, or we can also modify the width/length of the MOS capacitor places between the output nodes, or we can also alter the number of parallel MOS caps we put it and combine them with standard capacitors placed in series.

All of these modifications are seen on the following circuits designed.

Oscillator at 2.0 gigahertz

At 2 GHz. (Figure 12) we require lower capacitances values in the LC-tank (Eq. 1) as the frequency increases. A set of NMOS in parallel with $W=10$ microns, $L=500$ nano is used as each of the crossed-coupled NMOS. To reach an overall reduction in C , the active transistors in the cross coupled array are reduced to four (in parallel) at each side (from initially ten in the 0.5 GHz to 1.75 oscillators). Also an array of two serialized MOS- caps are placed between the inductors to reduce further the overall capacitance. Limitations on the technology detail size prevent us to just decrease the L and W as we did before for the MOS capacitor. Twin caps to the side of the MOS -caps are tuned to 3.10pF. These are parametrical capacitors from Honeywell MOI5 library, and are named mimcaps. Vdd is set to 5 volts supply. Output waves can be seen in Figure 12. The outputs nodes are out of phase by 180 degrees (nodes of the internal capacitor between the inductors). One thing to notice is that the max amplitude of oscillator is being clipped just over the supply voltage. This will produce the non rounded top of the output wave, making it look trimmed.

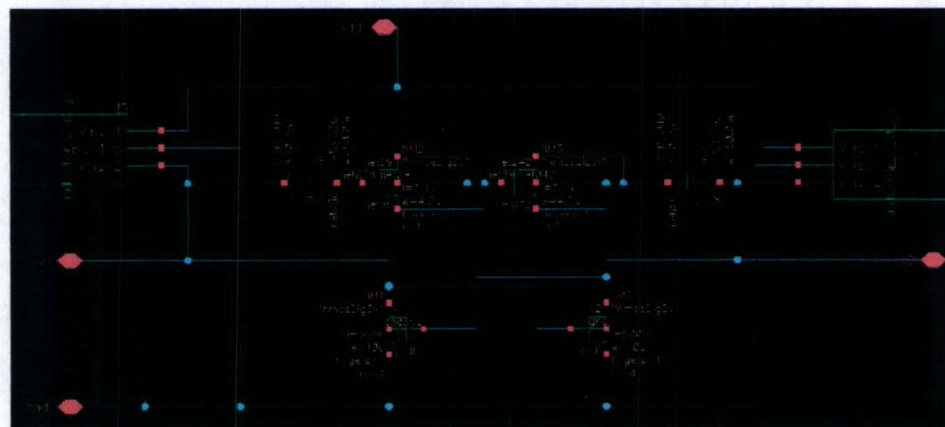


Figure 12: 2.0 GHz oscillator schematic

Oscillator behavior using ideal inductors

The following chart is presents a comparison of the performance of our thin-film oscillator with the thin film inductors an ideal inductor (pure inductance effects) placed in on the same circuit. As we can see a higher oscillation frequency is always reached with an ideal inductor (because of the lower overall C). The difference between the ideal and real inductor follows a tendency for our circuits which is shown on the plotted graph. Note the fourth column named “capacitance” which has the capacitance value “seen” by an inductor when is modeled as our physical cross-coupled oscillator. This capacitance is computed by usage of the reached oscillating frequency when we plug the ideal inductor and use the equation 1 to solve for C.

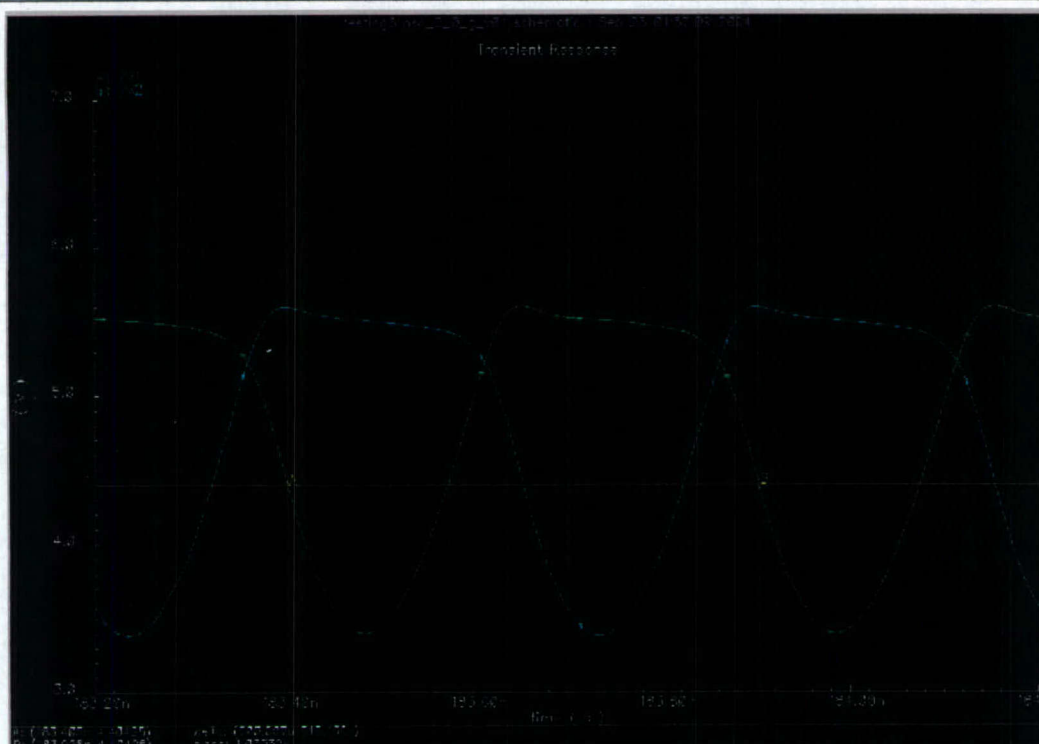


Figure 13: Oscillator output waveform

For getting a reasonable approach to a final oscillating frequency on intermediate inductor values for a fixed seen C value (given by the circuit) table II and Figure 14 can be used (re- placing with pure L as the complex L real model when designing).

Table II: variation on final oscillating frequency

Oscillator circuit type used (gigahertz)	Obtained freq with ideal inductor (Mhz)	Variation on frequency (%)	Capacitance seen by inductor (C) (pF)
0.5	505.2699657	1.05399315	5.3153401E-12
0.75	799.7440819	6.63254425	2.0842344E-12
1	1088.107313	8.81073135	1.0964164E-12
1.5	1709.901527	13.9934351	4.0849633E-13
1.75	2098.103105	19.891606	2.5532592E-13
2	2608.80681	30.4403405	1.5280218E-13

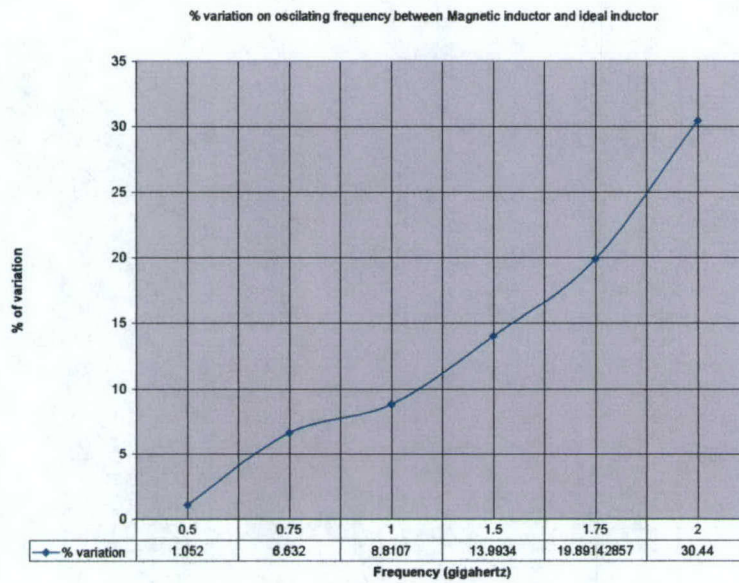


Figure 14: Frequency deviation from using ideal inductors.

III. Conclusions

The simulation data from HFSS tool was able to be migrated to the Cadence Virtuoso integrated circuit layout tool and the Spectre simulator, using Spectre's two port network representation of the inductors for fixed frequencies.

A set of circuits was designed to work with the modeled inductors for a range of frequencies (0.5 to 2.0 GHz). Oscillation over 2.ghz was difficult to reach with the cross coupled topology oscillators.

The set of circuits designed here would respond with a variation tendency (in the frequency output) to a change in the capacitance or the inductance parameter, which can be used to infer real capacitance and inductance that the manufactured thin film inductor is reaching.

When we are able to fabricate physical inductors, we will use a test circuit such as this one to characterize them on-chip.